



**HAL**  
open science

## Multiscale Visualization and Quantification of the Effect of Binders on the Acidity of Shaped Zeolites

Koen Kennes, Alexey Kubarev, Coralie Demaret, Laureline Treps, Olivier Delpoux, Mickael Rivallan, Emmanuelle Guillon, Alain Méthivier, Theodorus de Bruin, Axel Gomez, et al.

► **To cite this version:**

Koen Kennes, Alexey Kubarev, Coralie Demaret, Laureline Treps, Olivier Delpoux, et al.. Multiscale Visualization and Quantification of the Effect of Binders on the Acidity of Shaped Zeolites. *ACS Catalysis*, 2022, 12 (11), pp.6794-6808. 10.1021/acscatal.2c02152 . hal-03715021

**HAL Id: hal-03715021**

**<https://ifp.hal.science/hal-03715021v1>**

Submitted on 6 Jul 2022

**HAL** is a multi-disciplinary open access archive for the deposit and dissemination of scientific research documents, whether they are published or not. The documents may come from teaching and research institutions in France or abroad, or from public or private research centers.

L'archive ouverte pluridisciplinaire **HAL**, est destinée au dépôt et à la diffusion de documents scientifiques de niveau recherche, publiés ou non, émanant des établissements d'enseignement et de recherche français ou étrangers, des laboratoires publics ou privés.

# Multiscale Visualization and Quantification

## of the Effect of Binders on the Acidity of Shaped Zeolites

Koen Kennes,<sup>[a,b]</sup> Alexey Kubarev,<sup>[a]</sup> Coralie Demaret,<sup>[b]</sup> Laureline Treps,<sup>[b]</sup> Olivier Delpoux,<sup>[b]</sup>  
Mickael Rivallan,<sup>[b]</sup> Emmanuelle Guillon,<sup>[b]</sup> Alain Méthivier,<sup>[b]</sup> Theodorus de Bruin,<sup>[c]</sup> Axel  
Gomez,<sup>[b,d]</sup> Bogdan Harbuzaru,<sup>[b]</sup> Maarten B.J. Roeffaers\*<sup>[a]</sup> and Céline Chizallet\*<sup>[b]</sup>

[a] Centre for Membrane separations, Adsorption, Catalysis and Spectroscopy for sustainable solutions, Faculty of Bioscience Engineering, KU Leuven, Celestijnenlaan 200F, 3001 Leuven, Belgium

[b] IFP Energies nouvelles – Rond-Point de l’Echangeur de Solaize – BP 3 69360 Solaize, France

[c] IFP Energies nouvelles, 1 et 4 avenue de Bois-Préau, BP3, 92852 Rueil-Malmaison, France

[d] Département de Chimie, École Normale Supérieure, PSL University, 75005 Paris, France

## **Abstract**

Shaping is a crucial step in the preparation of catalysts at the industrial scale, but a rationalized understanding of how binders impact the catalyst's performance is still far from apparent. In this work, the effect of shaping with common binders (boehmite,  $\gamma$ -Al<sub>2</sub>O<sub>3</sub> and silica) on the acidity and catalytic properties of an acid zeolite catalyst, H-ZSM-5, is probed. The zeolite-binder samples (1:1 ratio) are shaped following commonly employed procedures and analyzed using both conventional characterizations of the acidity and porosity as well as using advanced fluorescence microspectroscopic characterization. In the latter approach, the fluorescence intensity stemming from the Brønsted acid catalyzed furfuryl alcohol oligomerization is used to determine in detail the effect of shaping on the acid zeolite's catalytic activity. Through density functional theory (DFT) calculations the observed changes in catalytic performance are assigned to atomic-scale processes such as the interaction of acid sites with binder related molecular species and the migration of ions. The most detrimental effects related to shaping are migration of cations, e.g. Na<sup>+</sup>, from the binder to the zeolite, which is an important mechanism for silica binders, as well as pore blockage by alumina and silica species. Strong acid sites are also likely to be converted into weak ones upon interaction with binders. A counterbalancing effect is the genesis of some additional bridging OH groups upon filling of local defects with alumina species from alumina binders. With such knowledge in hand, it becomes possible to balance these effects to get the desired properties.

**Keywords:** zeolite, shaping, alumina, silica, fluorescence microscopy, density functional theory

## 1. Introduction

Zeolites, and more particularly H-ZSM-5, are widely used and studied as acid catalysts in a large range of laboratory scale reactions and processes relevant to the (petro)chemical industry<sup>1</sup> and for biomass conversion.<sup>2</sup> For their integration in industrial processes, the zeolite catalysts need to be shaped into pellets, tablets, etc.<sup>3-5</sup> However, due to the poor self-binding properties of zeolites, binders are typically added to allow the formation of the desired catalyst size and shape and to improve the mechanical strength of the material.<sup>6-8</sup> The most widely used binders are based on silica and alumina. Although previously assumed to be inert in the catalytic process, it has become clear that the binder can modify the acidity and hence the catalytic performance of the shaped zeolite catalyst.<sup>9,10,11,12-16</sup> Obtaining detailed knowledge of the interaction modes between binders and zeolites would be a strong asset in the prediction of the consequences of shaping on the performance of the catalyst. Since most zeolite catalysts are chosen and optimized before shaping, such knowledge is key to anticipating the final properties of the industrial catalyst.

However, the literature dealing with zeolite shaping and binder effects is not abundant, probably due to historical reluctance for sharing industrial know-how. This trend has changed in recent years. In early studies, bulk techniques such as temperature-programmed desorption (TPD)<sup>17</sup> and Fourier-transform infrared (FTIR) spectroscopy with probe molecules like pyridine<sup>7,13,18</sup> have been used to quantify the effects of the binder on the acidity of the embedded zeolite catalysts. Recently, several studies on fluid catalytic cracking catalysts have directly assessed the binder effect on the acidity of zeolites in a spatially resolved manner by fluorescence microscopy.<sup>13,19-20</sup> The use of fluorogenic probe reactions like the acid catalyzed oligomerization of furfuryl alcohol allows to identify and localize the Brønsted acid sites that actively participate in the catalytic process.<sup>21-22</sup> This is a highly complementary approach to TPD techniques, which indirectly quantify the global number of acid sites, as it also gives

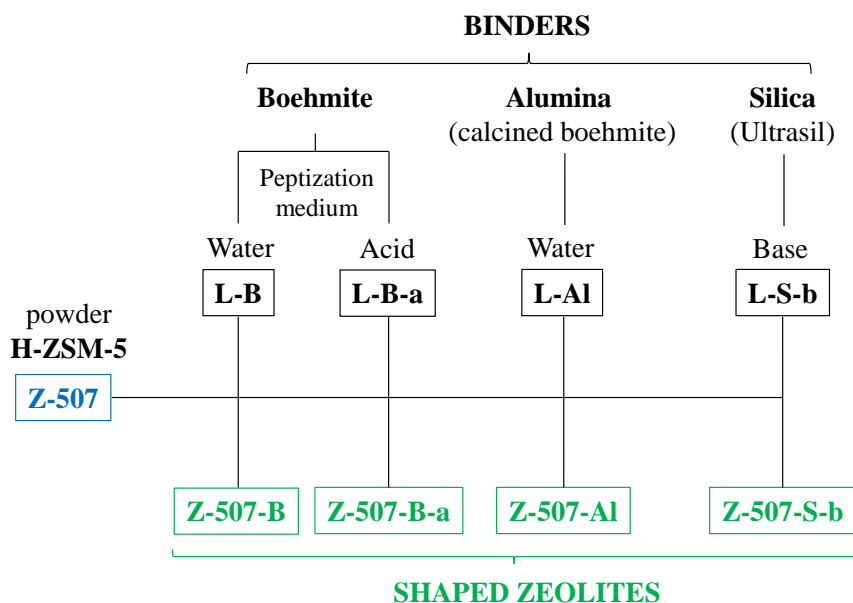
information on the relative accessibility of active sites. The use of bulky probe molecules, often monitored by FTIR, also allows to distinguish accessibility variations however in an indirect fashion.<sup>23</sup> Furthermore, in comparison to bulk scale FTIR and TPD techniques, fluorescence microscopy has a higher sensitivity enabling data collection at the single catalyst pellet level. For this reason fluorescence microscopy with fluorogenic probe reactions should enable to resolve i) binder effects that are typically lost in bulk-scale characterization and ii) modifications in catalytic activity at the scale of individual binder-embedded zeolite catalysts.

The main mechanisms of zeolite acidity modification during shaping that have been discussed in literature depend on the binder nature: dealumination,<sup>6,13,24-26</sup> realumination,<sup>11,16,20,27-29</sup> neutralization of acid sites<sup>6,30</sup> with cationic species, and pore blocking by extraframework Al species,<sup>31</sup> among others, are likely to take place. In this work, binder effects on the catalytic activity of acid zeolites were unravelled using an aluminium-poor H-ZSM-5 (Si/Al = 507) as reference material. By using aluminium-poor zeolites as reference material, the suggested binder effects should each have a very pronounced effect on the catalytic performance; the very low amounts of Brønsted acid sites, are however challenging to study with current state-of-the-art bulk-scale characterization techniques used in catalysis research. To overcome this hurdle, fluorescence microscopy was used. For this shaped, aluminium-poor reference zeolite material confocal laser-scanning microscopy (CLSM) is used to evaluate the catalytic activity distribution within full zeolite-binder pellets. As the catalytic activity is limited to zeolite nanocrystals, it allows the observation of the zeolite nanocrystals' distribution within the pellets. Additionally, traditional characterization techniques such as nitrogen physisorption were used to characterize the textural properties of the pellets.

Shaping of the H-ZSM-5 zeolite was performed with archetypical binders employed in industry (e.g. for catalytic cracking<sup>32</sup> and hydrocracking<sup>33</sup> processes): boehmite,  $\gamma$ -Al<sub>2</sub>O<sub>3</sub> (calcined boehmite) and silica (scheme 1). Additionally, the effect of peptization in an acidic

medium during shaping with boehmite was investigated, as this step is known to play an important role when shaping with boehmite;<sup>34-35</sup> peptisation of boehmite influences (1) the mesopores size, (2) the mechanical strength of the extrudates and (3) also yields a better dispersion of the active phase. The acid catalyzed furfuryl alcohol (FFA) oligomerization reaction was used to probe the catalytic activity in a spatially resolved fashion at the pellet scale using CLSM, and at the individual zeolite crystal scale using nanometer accuracy by stochastic chemical reactions (NASCA),<sup>19,36-40</sup> a super-resolution fluorescence microscopy approach.

Finally, to rationalize at the atomic scale the observed binder effects on the catalytic performance, density functional theory (DFT) calculations were made. Whereas the simulation of perfect zeolite catalysts is commonly reported, the studies dealing with zeolites containing defects, and including the behaviour of the external surface of the crystals, are much less abundant.<sup>41-42</sup> To the best of our knowledge, the effect of the binder was never considered in DFT simulations. In present work, using recently developed models,<sup>43-44</sup> migration of Na<sup>+</sup> ions from the silica binder to the zeolite, as well as pore blockage by alumina, and to some extent silica, species, are found to be detrimental to the catalytic performance of H-ZSM-5. The genesis of some new bridging OH groups upon filling of local defects with alumina species from alumina binders is seen to have a counterbalancing effect.



**Scheme 1** Used zeolites, binders and resulting samples.

## 2. Materials and methods

### 2.1. Zeolite material and pellet preparation

Zeolites were shaped in the form of pellets (diameter: 1 mm, length: 5 mm), into two steps: kneading (Brabender N50 with cam mixer blades) followed by piston extrusion (ERMA). ZSM-5 zeolite powder with a Si/Al ratio of 507 provided from Zeolyst (CBV1002) was mixed with the different binders at a fixed 1:1 mass ratio before shaping. The unshaped zeolite is called Z-507 in the following (scheme 1).

Shaping with boehmite was performed starting from a Pural SB3 precursor from Sasol, either in the presence of water (Z-507-B) or with a nitric acid solution (4 wt.% with respect to the peptisable boehmite weight) for peptization (Z-507-B-a). In the latter case, after 30 minutes of kneading, an  $\text{NH}_4\text{OH}$  solution (17 wt.%) is added for neutralization and further kneading for 15 minutes. For the shaping with  $\gamma\text{-Al}_2\text{O}_3$ , the boehmite powder was first calcined (2h at  $600^\circ\text{C}$ ), and then kneaded with the zeolite and water (Z-507-Al). Ultrasil (Evonik, sodium content: 4750

ppm) silica was chosen for the silica-ZSM-5 pellets (Z-507-S-b). The kneading step was performed in the presence of tetraethyl ammonium hydroxide (35 wt.% TEAOH solution in water) with a molar ratio  $\text{SiO}_2/\text{TEAOH} = 120$ . Pure binders were also shaped to give reference samples, their shaping follows the same procedure as the one used for the zeolite-binders composites. Their name is given in Table 1.

The extrusion was done thanks to a piston extruder (ERMA). Then, the pellets were dried at 80°C for 12h, cut to get 5 mm long pellets, and calcined under air at 600°C for 2h (ramp: 5°C/min).

## **2.2. Standard zeolite characterizations and catalytic testing**

### **N<sub>2</sub> physisorption**

A Micromeritics 2020 ASAP gas adsorption analyzer was used for nitrogen sorption measurements. Before analysis, the samples were outgassed for 1h at 100°C and for 4h at 500°C under vacuum ( $1.10^{-5}$  mbar). The total surface area ( $S_{\text{BET}}$ ) was determined from the BET equation. The t-plot method was used to obtain the microporous volumes and the  $S_{\text{ext}}$  (surface excluding the contribution of micropores). The micropore surface ( $S_{\mu}$ ) is the difference between the  $S_{\text{BET}}$  and  $S_{\text{ext}}$  of the samples.

### **Hg intrusion**

The mesoporous and macroporous volumes of the catalysts are obtained by mercury intrusion. This method is based on the non-wetting behaviour of the mercury for the solids. The pore size can be determined based on the external pressure needed to force the mercury into a pore against the opposing force of the mercury surface tension. The contact angle of the mercury with the pore walls is considered to be 140°. The technique is normally used for pores with a



diameter greater than 3.7 nm. The samples are pre-treated 4h at 250°C and the analysis is made on an Autopore IV 9520 (Micromeritics).

### **FTIR of OH groups and adsorbed pyridine**

In situ Fourier Transform Infra-Red (FTIR) spectroscopy was performed using a Nexus (ThermoOptek Nicolet) spectrometer. All the spectra were recorded at a resolution of 4 cm<sup>-1</sup> and 32 scans. The zeolites were pressed into self-supported wafers which were placed into an IR cell and treated in situ at 723 K during 10h under secondary vacuum (10<sup>-6</sup> mbar). The spectrum of the sample was then recorded to analyze the OH groups in presence. Pyridine was then introduced in contact with the sample (ca. 20 mbar equilibrium at room temperature). The concentrations of Brønsted Acid Sites (BAS) and Lewis Acid Sites (LAS) after thermodesorption of pyridine (at 423 K for 2h) are obtained using the molar extinction coefficients for the bands at 1545 and 1450 cm<sup>-1</sup> which are respectively 1.67 cm<sup>-1</sup>×μmol<sup>-1</sup> and 2.22 cm<sup>-1</sup>×μmol<sup>-1</sup>.<sup>45</sup>

Fourier self-deconvolution (FSD) of the IR spectra was performed on Thermo Omnic software in the 4000–3000 cm<sup>-1</sup> spectral range, using a line bandwidth of 20 cm<sup>-1</sup> (width of the contribution at the half-height) and an enhancement factor of 1 (ratio of the bandwidth before and after FSD treatment).

### **Meta-xylene isomerization catalytic test**

The isomerization of meta-xylene was carried out in a fixed-bed reactor at 300°C with a weight hourly space velocity of 1.2 h<sup>-1</sup>. Before the measurement, the samples (50 mg) were activated at 300°C under air for 2h. The effluent was analyzed by gas chromatography (Agilent, HP6580 with an FID detector and an FFAP column, 50 m (L) x 0.32 mm (ID) x 0.5 μm (thickness)).

### **2.3. Fluorescence microscopy experiments**

The glass cover slides (22x22 mm, #1) were calcined at 500°C and treated in an ozone reactor (Ultra violet products, PR-100), before the sample was drop casted on cover slides from an aqueous suspension of 10 mg crushed pellet in 10 mL Milli Q (Synergy UV, Merck Millipore). Subsequently, the cover slides containing the sample are calcined in a muffle furnace (Nabertherm LVT3/11) to remove any organic contaminants. This calcination is performed using the following heating program which allows removing the contaminants while minimizing alterations to the sample. First, the sample was heated at 1°C×min<sup>-1</sup> from room temperature to 80°C. This temperature was held for 1 hour, after which the sample was further heated to 120°C at 1°C×min<sup>-1</sup>. Again, this temperature was held for 1 hour, after which the temperature was further increased at 1°C×min<sup>-1</sup> to 450°C, where it remained for at least 48 hours. The coverslips with the sample were removed from the muffle furnace directly before the microscopy experiment to prevent unwanted contamination from the environment.

### **2.4. CLSM experiments**

The CLSM experiments were performed on an Olympus IX81 microscope equipped with a laser combiner and either 100×, 1.4 NA or 20×, 0.75 NA objective lens. The fluorescence signal is detected using a photomultiplier tube (PMT). The excitation laser light of 532 nm was filtered using a 535 nm dichroic mirror and a 545-645 nm emission filter. The pellets were added to a solution of FFA (4 vol%) in Milli-Q for 24 hours before being placed on a glass cover slide. For imaging of the full pellets, 141 subsequent 512 by 512 pixel images were taken spaced 0.25 μm in depth covering a total depth of 35 μm using a 20× objective. Full field-of-view images were stitched as 4×4 mosaic for every depth, resulting in 636×636 μm<sup>2</sup> images. For local areas imaging, separate 512 by 512 pixel images were taken by 100× objective at every 0.25 μm for a total depth of 15 μm (61 images), with a total field of view of 127×127 μm<sup>2</sup> area sizes. The

software package ImageJ was used to construct a 3D representation of these images. ImageJ was then used to calculate the average particle intensity of each particle.

## **2.5. Integrated light and electron microscopy**

To enable a straightforward correlation of structural information obtained by scanning electron microscopy (SEM) with single catalytic turnover activity maps obtained by NACSA microscopy, an integrated light and electron microscope was applied in this research. This integrated system is based on an FEI Quanta 250 FEG environmental scanning electron microscope in which the original SEM chamber door is replaced with the SECOM platform acquired from Delmic BV. The SECOM platform comprises a sample stage, capable of holding a high numerical aperture oil-immersion objective lens (Nikon plan APO VC 100 $\times$ , 1.4 NA), and an optically transparent window that allows excitation and fluorescence light to be guided into and out of the vacuum SEM chamber. This configuration makes it possible to first obtain structural images from the top of the sample and to consecutively perform wide-field fluorescence imaging from the bottom side. The fluorescence imaging is achieved by using excitation light at 532 nm provided by an Omicron Laser hub, which is guided towards the objective lens by 442/532 nm dichroic mirror and filtered out before detection with a 542 nm long-pass filter. Due to the vacuum conditions in the sample chamber during SEM imaging, a vacuum compatible immersion oil (1-Ethyl-3-methylimidazolium acetate (BASF)) was used. An EMCCD camera (Hamamatsu C9100-23B, 512x512 pixels) is positioned on the outside of the SEM door to detect the emitted fluorescence signal. The optical pathway in our specific system differs from the standard SECOM platform, as it was optimized for single-molecule detection.

## 2.6. NASCA experiments

The acquired wide-field fluorescence microscopy movies were analysed using the Localizer plug-in for Igor Pro (Wavemetrics).<sup>46</sup> Localizer is available online (<https://bitbucket.org/pdedecker/localizer>) and is applied to localize the individual fluorogenic turnovers and accumulate them into the NASCA activity maps. As such, the activity maps contain all turnovers that occurred over the course of the movie and within the focal plane, which is typically positioned in the middle of the crystals. After the turnovers are accumulated, identical emitters in consecutive frames are removed by position consolidation.

## 2.7. DFT calculations

Periodic DFT calculations were performed with the PBE (Perdew, Burke, and Ernzerhof) exchange-correlation functional<sup>47</sup> with VASP 5.4.1.<sup>48-49</sup> The projected augmented wave (PAW) method<sup>50</sup> was used to describe the core-electron interactions. The plane wave basis set was limited to a kinetic cutoff energy of 400 eV. A density dependent dispersion correction, dDsC,<sup>51</sup> was applied. The convergence criterion for the electronic self-consistent field relaxation was fixed to  $10^{-5}$  eV. All calculations were performed at the  $\Gamma$ -point, except for the (100) surface models where a  $1 \times 1 \times 2$   $\mathbf{k}$ -point mesh was used. Full geometry optimizations were performed using a conjugate-gradient algorithm, with a convergence criterion on forces of  $0.02 \text{ eV} \times \text{\AA}^{-1}$ .

Models for the H-ZSM-5 zeolite surfaces were taken from ref. <sup>43-44</sup> The amorphous silica surface model obtained by Tielens et al.<sup>52</sup> was considered as a starting point for the investigation of the interaction with sodium, with the following cell dimensions:  $a = 12.775 \text{ \AA}$ ,  $b = 17.636 \text{ \AA}$ ,  $c = 25.173 \text{ \AA}$ .  $\gamma\text{-Al}_2\text{O}_3$  surface models by Digne et al.,<sup>53-55</sup> constructed along the (110) and (100) orientations, were also computed for comparison.

### 3. Results

#### 3.1. Conventional porosity and acidity characterization

The porous properties of unshaped and shaped samples (50 wt.%) are reported in Table 1. The textural properties of the shaped binders were also measured as a reference, to deduce the deviation between the expected value and the measured one for shaped zeolites (Table 1). The adsorption isotherms are compared in Figure S1. The BET surface of the Z-507 sample is dominantly microporous, by contrast with that of the used binders.

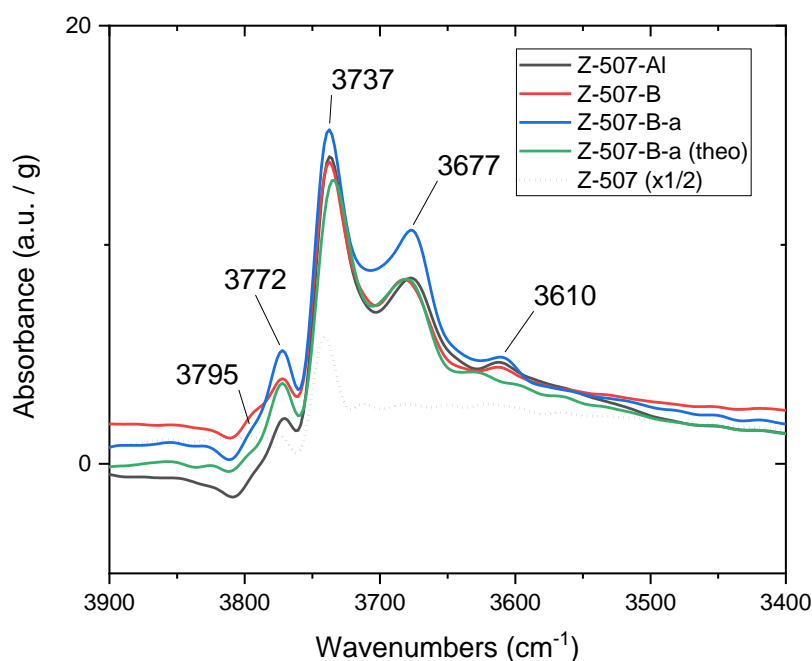
**Table 1.** Textural properties as measured by N<sub>2</sub> desorption and Hg intrusion experiments, Brønsted and Lewis acidities determined from pyridine-IR measurements. S<sub>BET</sub>, S<sub>μ</sub>, S<sub>ext</sub> are the BET, microporous and external (non-microporous) surface areas respectively, V<sub>μ</sub>, V<sub>meso</sub> and V<sub>macro</sub> are the microporous, mesoporous and macroporous volumes respectively. For the shaped zeolite samples, the deviation between the measured feature and the theoretical one (considering the features of the pure zeolite and the shaped binders, and the 1:1 ratio of zeolite and binder in the shaped zeolite samples) is given in parentheses.

Sample name	S <sub>BET</sub> (m <sup>2</sup> /g)	S <sub>μ</sub> (m <sup>2</sup> /g)	S <sub>ext</sub> (m <sup>2</sup> /g)	V <sub>μ</sub> (mL/g)	V <sub>meso</sub> (mL/g)	V <sub>macro</sub> (mL/g)	BAS (μmol/g)	LAS (μmol/g)
Z-507	371	307	64	0.116	0.02	-	5±3	17±5
Z-507-B-a	294 (-8%)	132 (-17%)	162 (+1%)	0.057 (-3%)	0.35 (-1%)	0.01	8±3	134±20
Z-507-B	286 (-9%)	127 (-19%)	159 (+1%)	0.057 (-3%)	0.34 (+10%)	0.08	8±3	94±15
Z-507-Al	268 (-9%)	128 (-18%)	140 (+2%)	0.056 (-4%)	0.21 (-9%)	0.20	8±3	104±15
Z-507-S-b	257 (-6%)	119 (-24%)	138 (+19%)	0.052 (-12%)	0.46 (-9%)	0.26	0	12±5
L-B-a	266	10	256	0.002	0.69	0.01	0	206±30
L-B	257	6	251	0.001	0.60	0.06	0	193±30
L-Al	217	7	210	0.001	0.44	0.15	0	217±30
L-S-b	173	6	167	0.002	0.99	0.20	0	0

The determination of the porous properties from N<sub>2</sub> physisorption for samples with micro-, meso- and macroporosity is a complex problem and the resulting values are strongly dependent on the chosen methods.<sup>56-57</sup> The t-plot method, routinely used in the field, and applied in present work is expected to lead to an under-estimation of the microporous volume V<sub>μ</sub>. Thus, only trends will be discussed, rather than absolute values. The microporosity is only insignificantly influenced by the shaping, and in the case of the silica binder micropore blockage seems apparent with 12% volume loss. The evolution of mesoporosity during shaping is much less systematic; for boehmite without acid peptization an increase in mesopore volume is observed while a loss in mesopore volume is observed for silica and alumina as binder. Note, however,

that mesoporosity is obtained by assembling grains of different sizes, inducing natural deviations with respect to the value obtained by a linear combination of the mesoporous volumes of the binder and that of the zeolite.

Surface hydroxyls of Z-507 based samples have been characterized by infrared spectroscopy. IR spectra have been mathematically treated by Fourier Self Deconvolution (FSD) to better depict the subtle differences between the samples in the hydroxyl region (Figure 1 for the boehmite and alumina shaped samples, Figure S2-B for the silica-shaped series). In addition, a theoretical spectrum of Z-507-B-a sample (in green) has been calculated from the combination of experimental IR spectra of Z-507 and L-B-a, accounting for the zeolite:binder 1:1 ratio in the pellets.



**Figure 1.** FSD-IR spectra of Z-507 based samples in the hydroxyl region after thermal activation at 723 K under secondary vacuum. Z-507-B-a (theo) (in green) calculated spectrum corresponds to a linear combination of experimental Z-507 (x 1/2) (dot) and L-B-a (x 1/2) spectra (not shown). Z-507 spectrum is reported in dotted line for 500 mg of Z-507, ie at similar Z-507 content than other samples.

For the Z-507 boehmite and alumina shaped samples, 5 main spectral contributions are visible, stemming from the presence of different hydroxyl species located on the surface of alumina binder and zeolite crystals. The bands at 3795, 3772, 3677 cm<sup>-1</sup> are assigned to

aluminol species ( $\text{OH-}\mu_1\text{-Al}_{\text{IV}}$ ,  $\text{OH-}\mu_1\text{-Al}_{\text{VI}}$ ,  $\text{OH-}\mu_2\text{-Al}_{\text{VI}}$  respectively<sup>54</sup>) while the band at  $3737\text{ cm}^{-1}$  is related both to silanol groups and  $\text{OH-}\mu_1\text{-Al}_{\text{V}}$ .<sup>44,54,58</sup> In addition a weak contribution at  $3610\text{ cm}^{-1}$  is present for all Z-507 alumina shaped samples, assigned to the acid bridging Si-OH-Al groups,<sup>18</sup> which is absent in the parent Z-507 sample as well as in the binder. This may imply the moderate alumination of the Z-507 framework during the kneading-extrusion process. For the silica shaped sample (Figure S2), the main feature shown by FTIR is the predominance of silanol groups in the sample, without any appearance of any other specific OH group.

After thermal activation, pyridine adsorption and following desorption at 423 K were then performed for all samples to quantify the various kinds of acid sites: Lewis and Brønsted (LAS and BAS, Table 1). For the pure Z-507 zeolite, the amount of detected BAS of about  $5\text{ }\mu\text{mol/g}$  is close to the detection limit and far below the theoretical value of  $32\text{ }\mu\text{mol/g}$ , calculated from the Si/Al ratio. This also means that it is difficult to detect a loss in acidity after shaping as for the shaped samples, half of this concentration is *a priori* expected, since the binders are not exhibiting any BAS, and the pellets contain 50 wt% zeolite. However, interestingly, the pyridinium ion signal on boehmite and alumina shaped samples is more intense than that of the original Z-507 zeolite (Figure S2-B, Table 1). This result correlates well with the increasing concentration of bridging Si-OH-Al acid sites observed in the hydroxyl region (Figure 1) and is indicative of Al migration from the binder to the zeolite framework. On the other hand, no pyridinium ion signal is observed for silica shaped Z-507-S-b. While these measurements were operated close to the limit of detection, it does suggest a negative effect of the shaping on the acidity.

Finally, to detect acidity differences in the shaped zeolite samples, meta-xylene isomerization tests was performed. From the results reported in Figure S3, it can be seen that samples shaped with boehmite or alumina display a similar activity which is slightly higher

with respect to the parent zeolite, whereas shaping with silica leads to a significant reduction in acidity.

To conclude, the conventional characterization techniques reveal some trends in the effect of shaping on the acidity of the parent ZSM-5. Whereas aluminium-rich binders lead to an increased amount of acid sites, silica almost completely removes the acidity. The latter also leads to a reduction in microporosity which might indicate pore blockage.

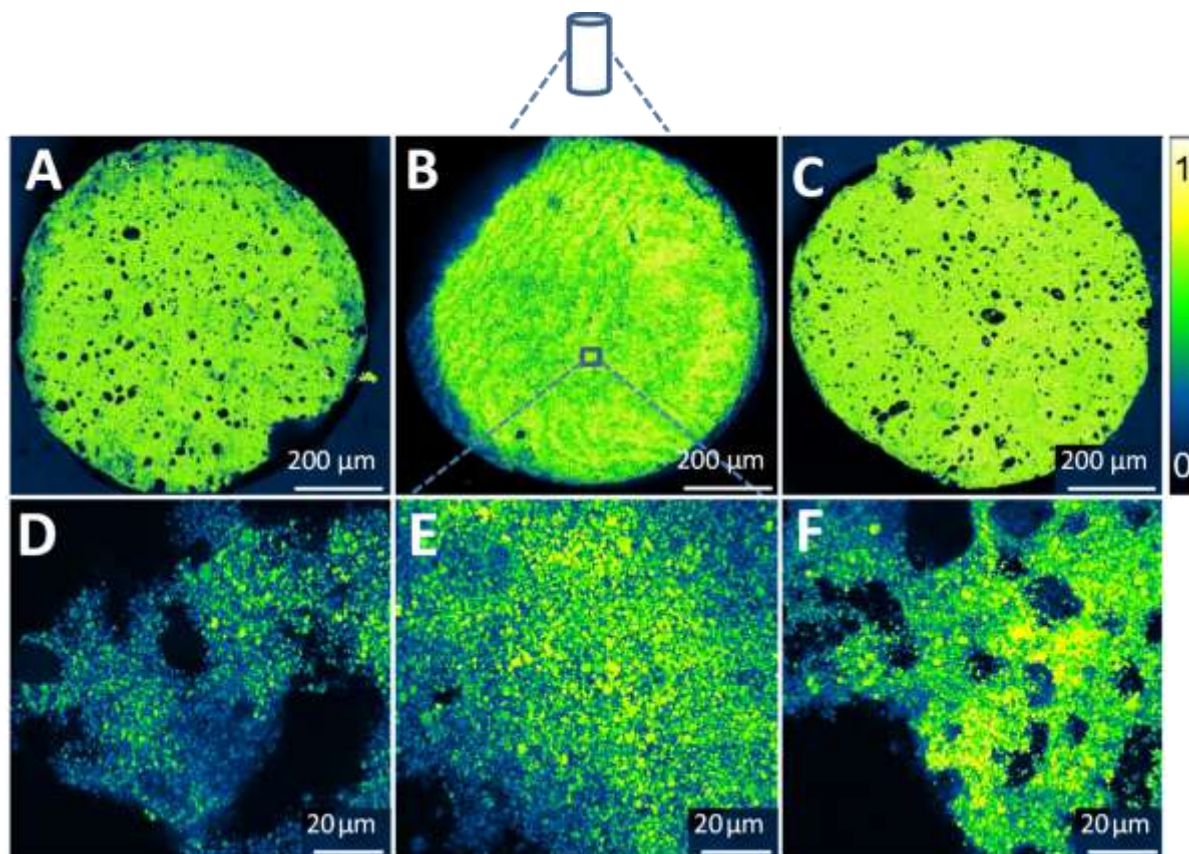
### **3.2. Probing the spatial distribution and catalytic activity of the acid zeolite particles after shaping using CLSM**

The effect of the binder and shaping procedure on the catalytic activity distribution was next examined at the full pellet scale using fluorescence microscopy. The pellets were submerged in an aqueous FFA solution (4 vol%) and were left to react for 24h at room temperature in the dark. Next, the pellets were broken in half perpendicular to their long axis and the freshly exposed surface was studied by placing these broken pellets vertically on a clean cover slide. The used probe, FFA, undergoes an acid-catalyzed oligomerization at the zeolite Brønsted acid sites leading to a colored fluorescent product.<sup>40</sup> For this particular experiment, the aqueous solution remains clear and colorless for the whole duration of the experiment from which we conclude that most of the fluorescent oligomers remain confined in the H-ZSM-5 pores; this is also in line with previous reports.<sup>21-22,59</sup> Hence, the fluorescence signal is representative of the number of oligomers locally formed and can be used to map out the catalytic activity.

As a reference measurement, the used binders were submitted to the same reaction conditions. After 24h, no fluorescence signal could be measured at the level of the support particles (boehmite, alumina or silica) nor in the supernatant. Next, the reactivity distribution throughout the whole cross-section (Figure 2) of the pellet was probed. The pellets were initially imaged with a 20× objective. Sixteen tile images, each 159×159  $\mu\text{m}^2$ , were combined to form the full overview image of the pellet cross-section of 636×636  $\mu\text{m}^2$  (Figures 2A-C). Next, a Z-



stack of 141 such slices spaced  $0.25\ \mu\text{m}$  was recorded for each sample in order to reconstruct the reactivity in a representative  $35\ \mu\text{m}$  thick slice of the intact pellet. Several areas inside the pellet were additionally probed with a  $100\times$  objective for high-resolution images (Figures 2D-F;  $127\times 127\ \mu\text{m}^2$  field-of-view using  $512\times 512$  pixels or  $248\times 248\ \text{nm}^2$  per pixel).

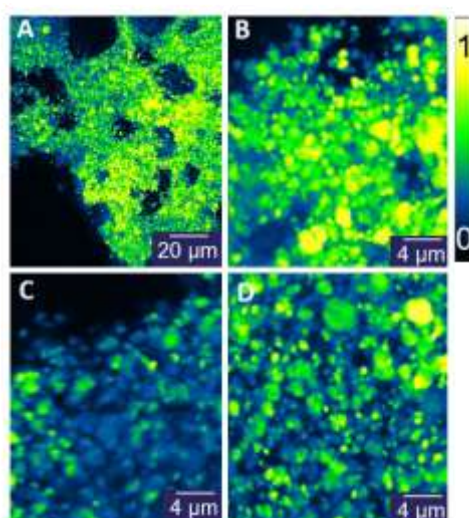


**Figure 2.** 2D projections of the activity assessed by measuring the fluorescence of the formed FFA oligomer over a depth of 35 (A-C) or 15 (D-F) microns of shaped Z-507 pellet using as a binder either A) boehmite, Z-507-B sample, B) peptized boehmite, Z-507-B-a sample, C) alumina, Z-507-AI sample. D-F) show the respective high-magnification, high-resolution activity maps of local areas of the pellets. The colour scale represents the fluorescence intensity when excited at 532 nm (2 mW in focus).

It is important to keep in mind that the parent zeolite displays some intra-crystal heterogeneity. Indeed, populations of crystals with high and low activity and mesoporosity coexist in the same batch related to the preparation conditions.<sup>39</sup> Based on the measurements of the pure compounds (binder and zeolite), the fluorescence signals observed (green-yellow) in the shaped samples can be assigned to the location of catalytically active Z-507 zeolite crystals, While the dark zones are linked to the catalytically inactive binder fraction, catalytically inactive zeolite crystals and the macroporous voids. Such voids are indeed

abundant for samples shaped without boehmite peptization step (Z-507-B) or with alumina (Z-507-A1) (Figures 2A and C), in line with the presence of macropores as determined at the bulk scale (Table 1).

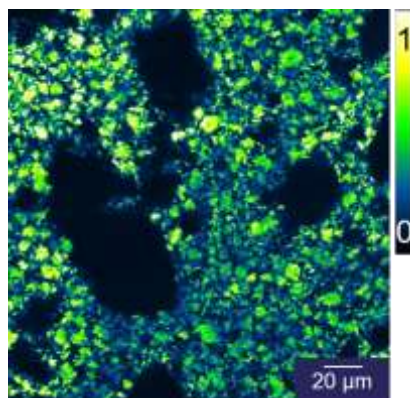
The fluorescent domains themselves show a distribution in fluorescence intensity. Several zones in the Z-507-A1 pellet (Figure 2F) were subjected to an additional 5X magnification which results in a 3D image of the zeolites within the pellet (Figure 3). In Figures 3B-D these zones are displayed as a 2D projection of the 3D images (see the electronic supporting information gif3D\_figure\_3A.gif and Gif3D\_figure\_3D.gif for 3D projections rotating around their central axis). In these projections, individual clusters of active zeolites can be seen, and the concentration and activity of these clusters vary significantly. There are several possible causes for this inhomogeneity in observed activity. To start with, the used Z-507 zeolite itself has a significant variation in catalytic activity.<sup>39</sup> Further, differences in molecular transportation throughout the pellet due to the binder, zeolite pore blockage and a spatially inhomogeneous effect of the binder on the zeolites are additional factors that need to be considered.



**Figure 3.** 2D projections of the activity assessed by measuring the fluorescence of the formed FFA oligomer over a depth of 15 micron of the Z-507-A1 sample pellet (A). Three areas were probed with an additional 5X zoom (B-D). The colour scale represents the fluorescence intensity when excited at 532 nm (2 mW in focus).

The comparison between the different binders learns that peptized boehmite yields the most homogeneous distribution of catalytically active zeolite crystals (Z-507-B-a sample, Figure 2B), while a more spatially heterogeneous distribution is seen in pellets made with boehmite and alumina as binders (Z-507-B and Z-507-A1 samples, Figure 2D, 2F). The peptization results in a better dispersion of the boehmite binder particles and in an increased mixing with the zeolite. Without peptization, binder particles cluster into aggregates spanning from several microns to several hundreds of microns in diameter.

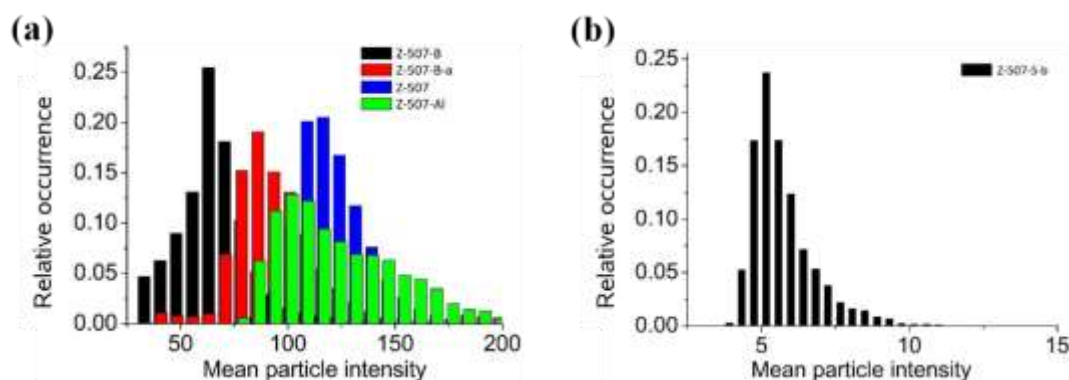
When silica was used as binder (Z-507-S-b) a strongly reduced fluorescence signal was observed and the laser power had to be increased seven-fold to record the shown data (Figure 4). This indicates a strongly negative effect of the silica binder on the acid zeolites which is likely due to i) the presence of sodium (4750 ppm) in the silica precursor which can exchange the acid Si-(OH)-Al Brønsted protons or ii) zeolite pore blockage by dissolved species originating from the binder and hindering the access to the active sites. For this binder, also an aggregation of particles and the presence of large voids are observed.



**Figure 4.** 2D projection of the activity assessed by measuring the fluorescence of the formed FFA oligomer over a depth of 15 micron of a Z-507-S-b pellet. The colour scale represents the fluorescence intensity when excited at 532 nm (14 mW in focus).

To quantitatively assess the binder effect on the catalytic activity, a detailed analysis of the fluorescence intensity of the zeolitic fraction in the 15 μm thick pellet slice was performed. Figure 5 shows intensity distribution histograms of the particles identified inside the shaped catalyst. With respect to pure Z-507, boehmite and alumina binders all result in a shift of the

distribution towards lower intensity, thus lower acidity, and in a broadening of the distribution (Figure 5-A). To check if these histograms represent different populations, we performed the Kruskal-Wallis ANOVA test which showed that between Sample Z-507-B and Sample Z-507-A1 there is a statistically significant different effect on the acidity of the embedded zeolites. Z-507-B is the most affected sample, whereas Z-507-A1 is closest to the original sample. Peptization of boehmite (sample Z-507-B-a) results in an intermediate situation.



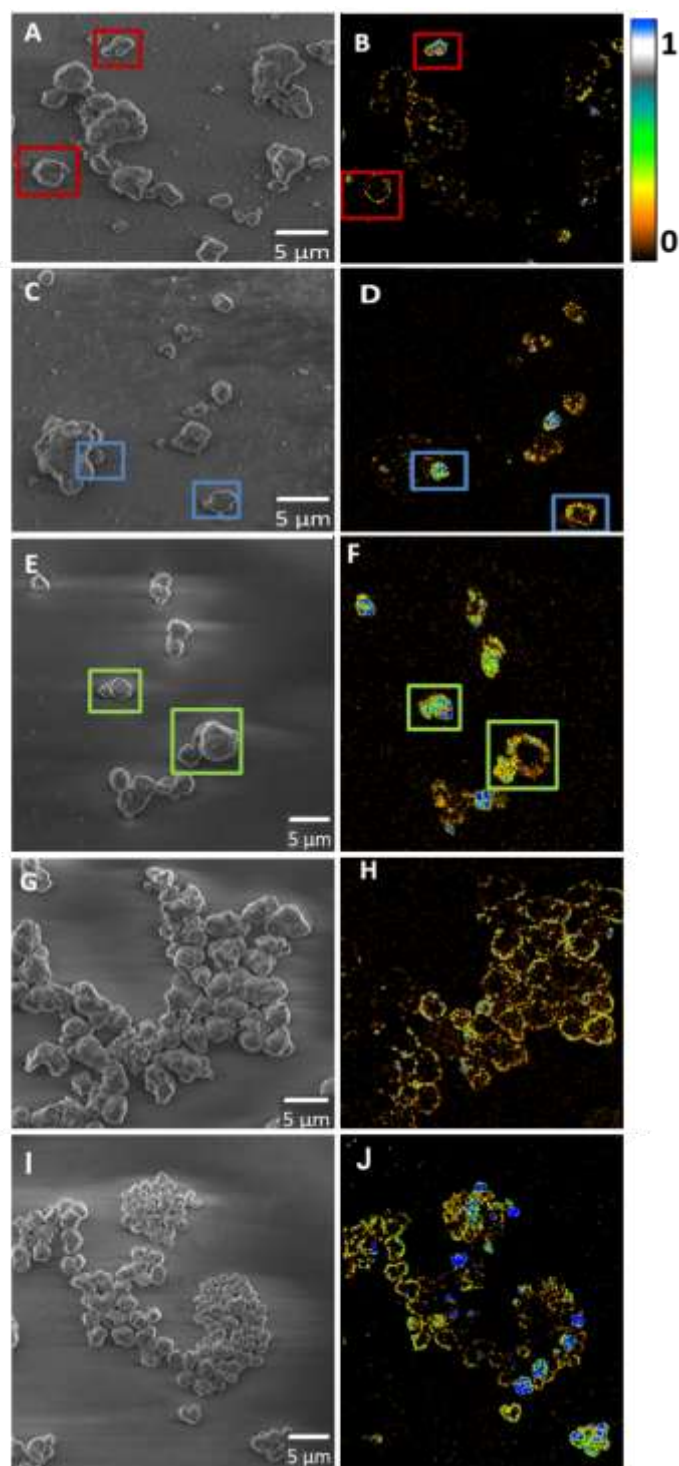
**Figure 5.** Histogram of the mean particle intensity of the fluorescent domains in figure 3 and 4. Excited at 532 nm, laser powers: 2 mW and 14 mW for the silica binder.

The measured fluorescence intensity, and thus catalytic activity, is lowest when a silica binder is used (sample Z-507-S-b, Figure 5-B). In comparison, samples shaped with boehmite and alumina binders show about 10-20 times higher catalytic activity. Thus, the quantification of the fluorescence intensity provides a much more precise method to rank the samples one with respect to the other, if we compare with traditional methods (table 1). Silica appears to have a dramatic effect on catalytic activity. At the individual particle level, shaping with alumina also decreases the acidity. Among boehmite and alumina shaped samples, peptization seems to be beneficial and both increase the mean catalytic activity and result in a much broader intensity distribution. Sample Z-507-A1 exhibits the most active zeolite domains.

### 3.3. Visualizing the binder effect on individual acid zeolite particles using NASCA

In order to further visualize the impact of the binder on the catalytic activity at the level of individual acid zeolite crystals, NASCA microscopy with single catalytic turnover sensitivity and improved spatial resolution was employed. To study the catalytic activity of the affected zeolites, pellets were gently crushed and sonicated in Milli-Q water to remove most of the outer binder shell allowing easier access to the zeolite. Next, they were drop-casted on a clean cover slide and calcined to remove possible fluorescent contaminations.

On the original Z-507 sample, several types of particles were observed by NASCA:<sup>39</sup> some exhibit a high catalytic activity homogeneously distributed throughout the whole particle volume, others only display activity at the outer rim of the crystals, and finally, the third group of particles displayed no measurable activity. The same three families are observed for samples shaped with boehmite and alumina binders (Z-507-B, Z-507-B-a and Z-507-Al, Figure 6A to F). In agreement with the CLSM data, zeolites that were bound with boehmite show a significant loss of activity compared to the pure zeolite.<sup>39</sup> Similar results are obtained for the Z-507-B and Z-507-B-a samples, but with a slightly higher final reactivity when boehmite is peptized (Z-507-B-a). The results for the zeolite shaped with alumina (Z-507-Al, Figure 6-E-F) are in strong contrast to those shaped with (peptized) boehmite. In this case, all observed crystals show higher activity, with a larger population of crystals that shine from their rim to their core. In conclusion, the number of fully active crystals can be ordered as a function of the used binder: Alumina (Z-507-Al) > peptized boehmite (Z-507-B-a) ~ boehmite (Z-507-B).



**Figure 6.** NASCA reactivity maps (right) and their corresponding SEM images (left) of alumina-poor H-ZSM-5 Z-507 zeolites shaped with different types of binders. A)-B) boehmite, Z-507-B, C)-D) peptized boehmite, Z-507-B-a, E)-F) alumina, Z-507-Al, and G)-H) silica, Z-507-S-b, I)-J) unshaped Z-507 reference sample.

For the Z-507-S-b sample, shaped with silica, when NASCA is performed using the same concentration of FFA as for the sample prepared from the pellets made with alumina binders,

almost no turnovers are observed, as expected from the CLSM measurements. Therefore the concentration of FFA was increased twofold in order to obtain the NASCA reactivity maps in Figure 6H. These particles (consisting out of 2 or 3 zeolite particles) show an activity exclusively on their combined edges: this is a strong indication that most acid sites located in the core of the crystals of Z-507 have been poisoned, while not all sites located at the rim have been poisoned (even if a large part of these have also been poisoned, as attested by the necessity of the FFA concentration increase). We suggest that this could be due to the migration of the sodium present in the silica binder into the zeolite crystals. Yet, we can also not exclude a pore blockage effect of silica, as attested by the loss of microporous volume (Table 1). DFT calculations reported in section 3.4 further substantiate the role of sodium migration from silica and the preferential poisoning of the core of the crystals.

### 3.4. DFT calculations

To better understand the experimental observations and give an atomic scale interpretation, we performed periodic density functional theory calculations, to unravel the interaction of bulk *versus* external surface sites with alumina and silica monomers, likely to be formed in the course of the shaping and to migrate in the pore system of ZSM-5, and with sodium ions (as they are likely to play a key role when silica is used as a binder).

- *Interaction of ZSM-5 with alumina and silica monomers*

Al(H<sub>2</sub>O)(OH)<sub>3</sub> and Si(OH)<sub>4</sub> monomers were considered, being the most simple models of species that may be formed in the medium from alumina and silica binders. Their interaction with various sites of the bulk and external surface of the zeolite was quantified thanks to the adsorption energy  $\Delta_{\text{ads}}U_{\text{monomer}}$  defined in equation (1).

$$\Delta_{\text{ads}}U_{\text{monomer}} = U_{\text{zeolite-monomer}} - U_{\text{zeolite}} - U_{\text{binder}} \quad \text{eq. (1)}$$

where  $U_{\text{zeolite-monomer}}$ ,  $U_{\text{zeolite}}$  and  $U_{\text{binder}}$  are the electronic energies of the zeolite interacting with the monomer, of the “empty” zeolite and the isolated monomer respectively.

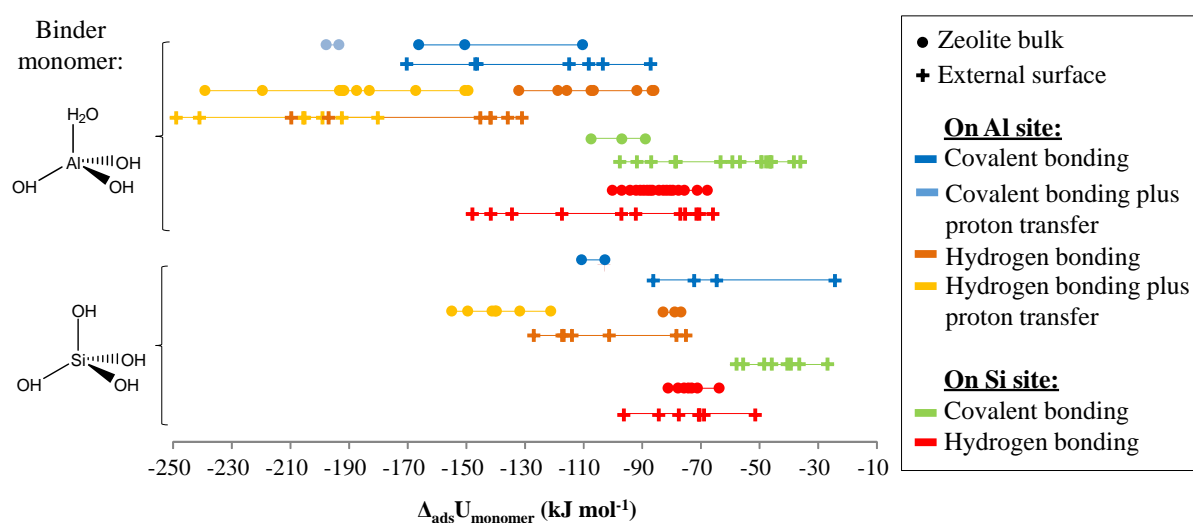
For the bulk site, the aluminium atom was placed at the T5 site, located at the intersection between the straight and sinusoidal channels. The (100) external surface models chosen<sup>43</sup> exhibit an Al-(H<sub>2</sub>O) as the most stable acid site. Numerous configurations were probed that can be classified into 3 main families, depending on the interaction mode with the framework: i) van der Waals and hydrogen bonding may result in non-covalent interaction, ii) in some cases binder monomers also form covalent bonds with framework atoms, iii) finally, proton transfer reaction from the zeolite to the binder monomer takes place in some cases. The results also depend on the nature of the framework sites undergoing such interactions (close to Si or Al atoms). Selected geometries are presented in Tables 2 (bulk sites) and S2 (external surface sites). Adsorption energies are gathered in Figure 7, details being given in Tables S1 and S2.

Generally speaking, the adsorption of the alumina monomer is stronger (strongest adsorption: -250 kJ/mol) than that of the silica monomer (strongest adsorption: -154 kJ/mol). Both for silica and alumina monomers, the adsorption around silicon sites (strongest adsorption: -150 kJ/mol) is generally weaker than close to aluminium (strongest adsorption: -250 kJ/mol).

For the alumina monomer, the most favourable adsorption modes correspond to hydrogen bonding plus proton transfer from the zeolite framework (example: configuration C in Table 2). This illustrates the basicity of the Al-OH group of the monomer, as already shown by Benco et al. in the case of gmelinite.<sup>60</sup> For this mode, interaction strength with the bulk and external acid sites is of similar intensity. The modes leading to the formation of covalent  $\text{Si}_{\text{framework}}\text{-O}_{\text{binder}}$  or  $\text{Al}_{\text{framework}}\text{-O}_{\text{binder}}$  correspond to a more moderate energy gain, but still with strongly negative adsorption energy, in particular when such a covalent bonding is accompanied by proton transfer (minimal values: -198 kJ/mol). When framework aluminium sites are



involved,  $\mu_2$ -OH ( $\text{Al}_{\text{IV}}(\text{OH})-\text{Al}_{\text{V}}$ ) are formed (configurations A and B in Table 2). In some cases, this is accompanied by the weakening of the Si-OH $\cdots$ Al bond, converting a bridging OH group into a pseudo-bridging silanol (configuration B in Table 2), as proposed by DFT for amorphous silica-alumina.<sup>61-63</sup> When framework silicon sites are involved, the reaction is less favourable (minimal value: -105 kJ/mol), which can be linked to the formation of pentahedral silicon (configuration E in Table 2), belonging to a  $\text{Si}_{\text{V}}(\text{OH})-\text{Al}_{\text{IV}}$  group. Configurations, where the alumina monomer is bonded to the framework through hydrogen bonds only, were also calculated and appeared to be much more stable at the external surface of the zeolite than in the bulk (Figure 7, Table 2 entries D and F), and more stable close to the framework aluminium site rather than to purely silicic zones, again as a consequence of the higher basicity of oxygen atoms close to framework Al atoms.

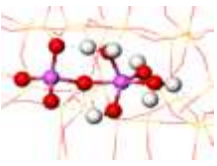
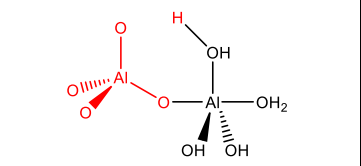
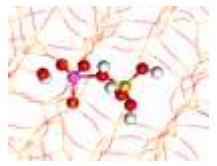
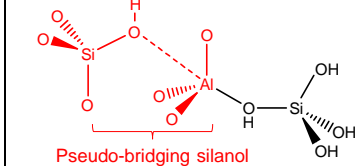
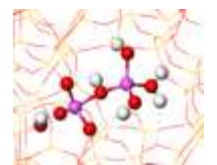
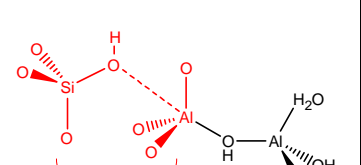
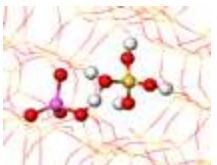
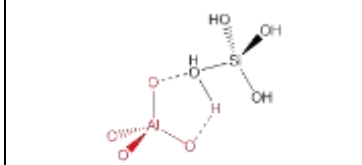

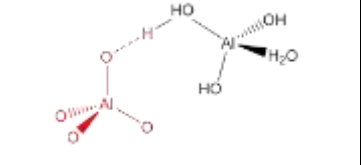
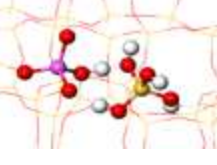
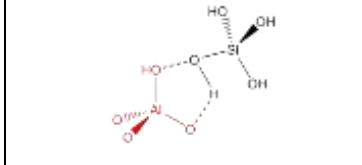
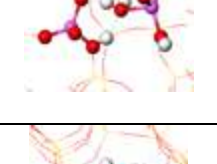
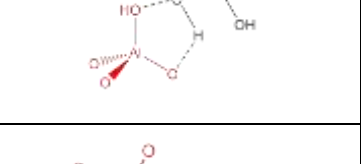

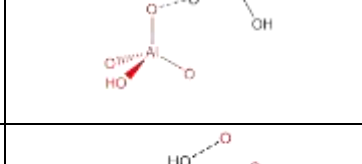

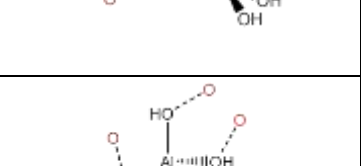

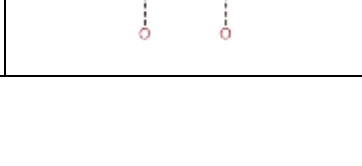




**Figure 7** DFT computed adsorption energies of alumina and silica monomers (kJ/mol) at the bulk and external surface sites of ZSM-5. For the external surface site, a selection of data is presented following various families given in Table S2, which also reports the exhaustive data.

Regarding the silica monomer, again the modes combining hydrogen bonding plus proton transfer from framework Brønsted acid sites (H in Table 2) are favoured. However, these modes are absent at the external surface, where the Brønsted acid site ( $\text{Al}(\text{H}_2\text{O})$ ) appears to be too weak to protonate Si-OH groups from the monomer. Thus, silica monomers interact more strongly with bulk sites rather than external surface sites, which could be at the origin of the

loss of the fluorescence at the core of the crystals shaped by silica, upon pore blocage by linker residues.

**Table 2.** Alumina (left) and silica (right) monomer adsorption representations in the bulk of ZSM-5 depending on the nature of the monomer, the adsorption site and the bond formed. (a) Ball and stick representation of the monomer and the adsorption site (Al: pink, Si: yellow, H: white, O: red), (b) Schematic representation of the adsorption, atoms originally from the zeolite network are represented in red, atoms originally from monomer are represented in black.

Name	Ball and stick view <sup>(a)</sup>	Schematic representation <sup>(b)</sup>	Name	Ball and stick view <sup>(a)</sup>	Schematic representation <sup>(b)</sup>
A			G		
B			H		
C			I		
D			J		
E			K		
F					

- *Exchange of Brønsted acid sites with Na<sup>+</sup>*

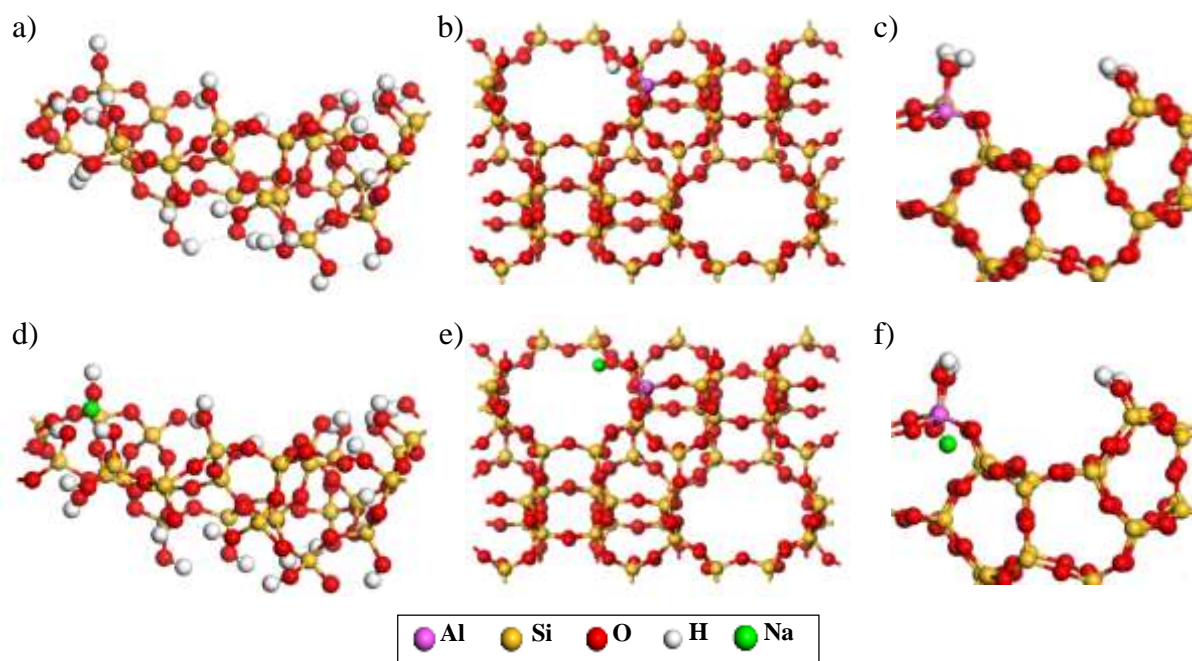
Since the experimentally employed silica sources hold a non-negligible sodium content, it is of interest to quantify the relative affinity of the sodium cations for the silica binder *versus* the zeolite. Therefore, we have constructed models for sodium exchanged silica, H-ZSM-5 (bulk and external surface). Starting from the amorphous silica surface model of Tielens et al.<sup>52</sup> (Figure 8-a), from H-ZSM-5 bulk models (Figure 8-b), and external surface models of H-ZSM-5,<sup>43</sup> exhibiting an Al-(H<sub>2</sub>O) as the most stable acid site (Figure 8-c), a set of H<sup>+</sup> → Na<sup>+</sup> exchange reactions (equation (2)) was simulated and their reaction energy was quantified.



Several exchange positions were sampled, Figures 8d,e,f depict the most stable ones. The corresponding exchange energies are -63 kJ/mol for the bulk H-ZSM-5 zeolite, *versus* -27 kJ/mol for the external surface site. Notably, the latter protonated model exhibits an Al-(H<sub>2</sub>O) site as the most stable Brønsted acid site, whereas the bulk zeolite model exhibits only Si-(OH)-Al sites. The negative exchange energies show that the affinity of the zeolite towards sodium is higher than that of the silica binder, meaning that sodium migration is expected to take place, on a thermodynamic basis. This favorable Na<sup>+</sup>/H<sup>+</sup> exchange is likely to explain the decrease of the activity measured by fluorescence microscopy in the Z-507-S-b sample, when compared to the Z-507 sample, as well as the loss of catalytic activity in xylene isomerization.

The comparison of the exchange energies for bulk and external surface models of ZSM-5 shows that the bulk bridging OH groups are more prone to be exchanged. The lower electrostatic field experienced at the external surface with respect to the bulk sites<sup>64</sup> might be the reason for the weaker interaction, as well as the different nature of the surface site (Al-(H<sub>2</sub>O) at the external surface, instead of bridging OH group within the bulk). This is also in agreement with the observation of a stronger decrease of the fluorescence intensity at the core of the crystals rather than at the rim sites for Z-507-S-b, although the definition of the external

surface by DFT is much more local (a few Å) than by fluorescence microscopy (rims bright over dozens of nanometers).



**Figure 8.** Surface models for a) silica, from Tielens et al.,<sup>52</sup> side view, b) bulk of the H-ZSM-5 zeolite, view along the sinusoidal channel, c) external surface of the H-ZSM-5 zeolite, side view, cut along the (100) orientation, from ref. <sup>43</sup>. Only the topmost atoms of the slab are shown. d), e) and f) show corresponding best models where one H<sup>+</sup> ion was exchanged with one Na<sup>+</sup> ion.

For comparison, we also computed the exchange energy starting from sodium-exchanged alumina,<sup>55</sup> or sodium exchanged aluminated amorphous silica. The later model was built by substituting one of the silicon atoms of the amorphous silica model by a {Al,H} pair. Results (Table S3 and Figure S4) show that sodium-exchanged alumina would also lead to poisoning of the H-ZSM-5 zeolite, but aluminated silica would lead to a strong decrease of the phenomenon. This illustrates the stronger sodium affinity for aluminosilicate solids in general, rather than pure silica or alumina, and opens perspectives to avoid sodium poisoning.

## 4. Discussion

To go one step further in the atomic-scale understanding, the experimental observations and the DFT data are linked together to determine which interaction mode leads to the observed acidity evolution, in combination with data from the existing literature.

### 4.1 Alumina binders

Regarding boehmite and alumina binders and corresponding shaping procedures (leading to the Z-507-B, Z-507-B-a and Z-507-A1 samples), and according to DFT calculations, considering the partial dissolution of alumina and the mobility of the formed species moving from the binder to the zeolite in the course of the shaping procedure, several phenomena take place.

#### *Pore blockage*

Pore blockage can be invoked from all the computed interaction modes of the defect-free zones of the zeolite with the dissolved binder monomers. Pore blockage is experimentally observed from nitrogen adsorption measurements (Table 1) and is likely stronger when the alumina monomer gets trapped inside the zeolite framework. At the external surface, the remaining translational degrees of freedom of the monomer may remain higher, thus giving the entering molecule the possibility to access the zeolite microporous volume and the acid sites.

#### *Genesis of weak acid sites*

Binder/zeolite interaction modes that involve proton transfer from the zeolite to the  $\text{Al}(\text{OH})_3(\text{H}_2\text{O})$  moiety (entries A and C in Table 2) are expected to convert strong acid sites into weaker ones, harboured by the  $\text{Al}(\text{OH})_2(\text{H}_2\text{O})_2^+$  species. These species play the role of the compensation cation, instead of  $\text{H}^+$ . The newly generated Al-(H<sub>2</sub>O) group is indeed a weaker

acid site with respect to the original Si-(OH)-Al group.<sup>43</sup> Upon activation,  $\text{Al}(\text{OH})_2(\text{H}_2\text{O})_2^+$  may be dehydrated into species such as  $\text{Al}(\text{OH})_2(\text{H}_2\text{O})^+$ ,  $\text{Al}(\text{OH})_2^+$ ,  $\text{AlO}^+$ . This overall process was proposed as the neutralization of the zeolite by aluminium species.<sup>30</sup>

In the mode depicted in entry B, a bridging OH group is converted into a Pseudo-Bridging Silanol, known to be a weaker acid site with respect to bridging OH groups,<sup>62,65-67</sup> but still able to dehydrate alcohols thanks to the synergistic effect of their Brønsted and Lewis acid moieties.<sup>68</sup> Moreover, the same covalent mode creates a new  $\mu_2$ -Al-OH group, which can be described as weak Brønsted acid sites, when found on  $\gamma$ - $\text{Al}_2\text{O}_3$ .<sup>54</sup> These sites are, however, not likely to catalyze alcohol dehydration.<sup>69-70</sup>

#### *Genesis of new bridging OH groups*

The mode depicted in entry E of Table 2 corresponds to the covalent interaction of alumina monomers with silicon-rich zones of the framework, which were initially not acidic at all. Upon the formation of a new Si-O bond, it generates a  $\text{Si}_V\text{-(OH)-Al}_{IV}$  group, which is highly likely to behave as an additional Brønsted acid site. Notably, these covalent interaction modes are also likely at the external surface of ZSM-5, according to our DFT calculations: this could be linked to the enrichment of acid sites at the external surface of zeolite Y with boehmite, reported recently by Lakiss et al.<sup>14</sup>

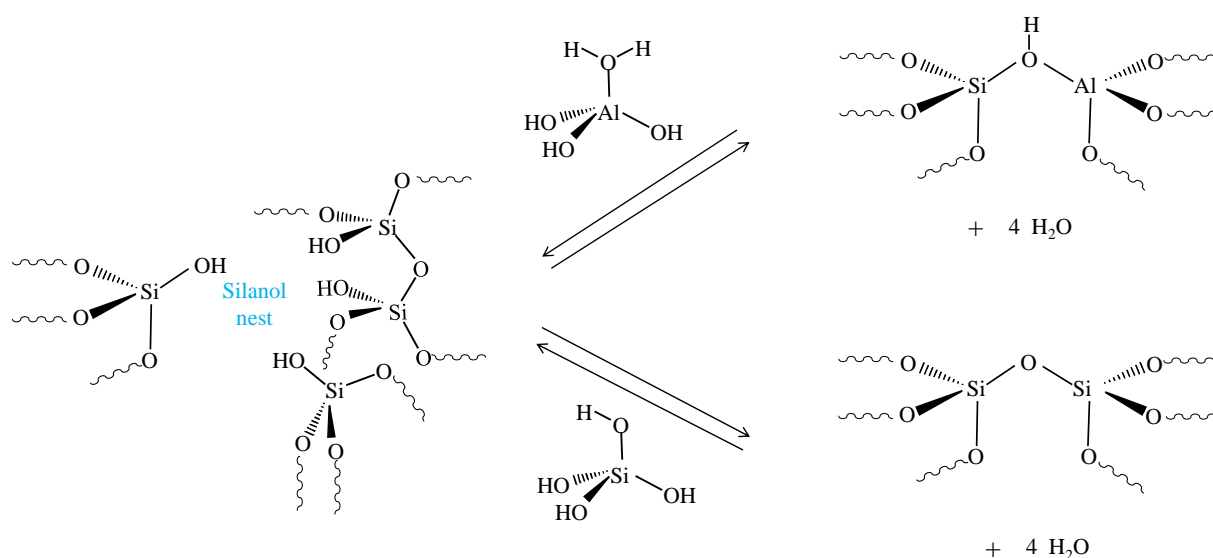
The filling of framework defects with alumina species may also be invoked. Quantified information can be obtained from previous DFT calculations dealing with the opposite process, namely the formation of an EFAl mononuclear species and a silanol nest, from a regular zeolite framework site. In the case of ZSM-5 as well as for other zeolites, the overall dealumination process was shown to correspond to a free energy loss,<sup>71-74</sup> meaning that alumination of silanol nests will correspond to a free energy gain, thanks to the release of four water molecules for each incorporated  $\text{Al}(\text{OH})_3(\text{H}_2\text{O})$  species (Scheme 2). This reaction also forms new Si-(OH)-

Al sites starting from a silanol nest (as suggested in the past for various zeolites shaped with aluminium-containing binders<sup>9,11,16,20,27-29</sup>), with a gain on Brønsted acidity, and a reduced pore blockage problem with respect to the interaction of the  $\text{Al}(\text{OH})_3(\text{H}_2\text{O})$  species with a defect-free zone.

The question about the balance between alumination and dealumination reactions needs to be raised. In the current situation, where an abundant alumina reservoir is put in contact with the zeolite, the balance between alumination and dealumination reactions is highly likely to be dominated by the former process. Another clue is that the dealumination of zeolite is often accompanied by the increase of the mesoporous volume, which is not the case here (Table 1).

Alumination may, however, take place only if kinetic limitations for the formation of alumina monomers can be overcome. This is likely what explains the differences observed between the Z-507-B, Z-507-B-a and Z-507-Al samples. Indeed, our simulations only consider a single species,  $\text{Al}(\text{OH})_3(\text{H}_2\text{O})$ , expected to be obtained upon alumina/boehmite dissolution (before thermal treatment) or as a consequence of thermal treatments (considering the mobility of some  $\text{Al}^{3+}$  ions, in particular when boehmite is transformed into  $\gamma\text{-Al}_2\text{O}_3$ <sup>75-76</sup>). Thus, the different properties exhibited by the Z-507-B, Z-507-B-a and Z-507-Al samples may be connected to the different monomer concentrations, depending on the chosen binders (boehmite,  $\gamma\text{-Al}_2\text{O}_3$ ) and shaping procedure (including peptization by nitric acid or not). Considering the higher activity observed for Z-507-Al (Figure 5), one may propose that higher numbers of monomeric species are formed when putting  $\gamma\text{-Al}_2\text{O}_3$  in contact with liquid water and the zeolite, than when starting from boehmite. It is indeed not a surprise that boehmite ( $\text{AlO}(\text{OH})$ ) is more stable in the presence of water than  $\gamma\text{-Al}_2\text{O}_3$ , the former being the hydrated form of the latter. Regarding the boehmite binder, it is expected that dissolution processes are more quantitative in the presence of nitric acid, favouring the hydrolysis of Al-O-Al bridges, on top of promotion of the dispersion of the boehmite aggregates. Thus, the alumination

processes (at the external surface of the zeolite, or defects sites of the bulk) are more likely during the preparation of Z-507-B-a than Z-507-B. Moreover, in the presence of nitric acid,  $\text{Al}(\text{OH})_3(\text{H}_2\text{O})$  likely is already protonated, limiting the extent of the proton transfer from the zeolite to  $\text{Al}(\text{OH})_3(\text{H}_2\text{O})$ . All this may explain the activity ranking between the two samples : Z-507-B-a > Z-507-B (Figure 5).



**Scheme 2.** Reaction equations involved in the incorporation of alumina (top) and silica (bottom) monomer at point defects of the zeolite. The reverse reactions are dealumination and desilication reactions respectively.

## 4.2. Silica binder

Regarding the silica-shaped sample (Z-507-S-b), a strong depletion of the acidity was observed when compared to the original Z-507 sample as well as compared to the alumina-shaped samples. Note that the effects of silica binders vary substantially in the literature, probably due to variations in silica source used but also the shaping procedures.<sup>6,9,20,30</sup> Similar to the case of boehmite and alumina binders, the question of the occurrence of dealumination may be raised, especially since in the case of silica, the aluminium reservoir is absent. Dealumination was indeed proposed as a possible origin of a drop in Brønsted acidity<sup>6</sup> or framework aluminium content<sup>24</sup> after shaping with silica. Although the basic medium involved at the beginning of the



shaping with silica should rather promote desilication,<sup>77</sup> gradient-driven dealumination may also be at the origin of the loss of acidity observed experimentally. Following our NASCA observations, it is, however, not clear why this should take place preferentially at the core of the crystals rather than at their rim. Thus, in the present case (ZSM-5, Si/Al = 507, shaped with ultrasil with TPAOH), dealumination is likely not the dominant phenomenon explaining the loss of acidity. Instead, we propose three mechanisms that likely take place in our case:

#### *Sodium exchange*

Sodium exchange was found to be thermodynamically feasible from an energetic point of view from our DFT calculations. Moreover, sodium interacts more strongly at internal porosity sites rather than at the external surface of ZSM-5. This is compatible with the observation of a stronger depletion of acidity in the core with respect to the rim of the zeolite crystallites. Poisoning of ZSM-5 by Na<sup>+</sup> cations from Na-containing montmorillonite binder was already shown in the past but without any spatial resolution of the phenomenon.<sup>78</sup>

#### *Pore blockage*

Similar to alumina monomers, all the other interaction modes of Si(OH)<sub>4</sub> with the zeolite framework may explain pore blockage, which is indeed observed by nitrogen adsorption measurements. The fact that bulk sites are the ones that lead to the strongest interaction with Si(OH)<sub>4</sub> moieties may explain the strong depletion of microporosity observed for the Z-507-S-b sample. The reverse trend was observed for alumina monomers, with a stronger interaction at the external surface of ZSM-5, likely to explain why the pore blockage phenomenon is more pronounced for Z-507-S-b than for the samples shaped with alumina and boehmite (Z-507-B, Z-507-B-a, Z-507-Al, Table 1). Should Si(OH)<sub>4</sub> be incorporated at the defects of the zeolite

framework, this could limit the pore blockage phenomenon but will have no impact on the Brønsted acidity (Scheme 2).

#### *Loss of strong Brønsted acid sites by proton transfer to binder monomers*

Our DFT calculations show that the most stable interaction mode of  $\text{Si}(\text{OH})_4$  with ZSM-5 is hydrogen bonding plus proton transfer from the bridging OH groups of ZSM-5 (H entry, Table 2). This was observed at the bulk sites only, the acidity of the external surface sites being far too low to generate a  $\text{Si}-(\text{OH}_2)^+$  species. Assuming that the formed  $\text{Si}(\text{OH})_3(\text{H}_2\text{O})^+$  is only a weakly acidic species, then the acidity depletion observed by fluorescence microscopy can be explained.

## **5. Conclusion**

Shaping an aluminum-poor zeolite (such as the Z-507 sample considered here, a ZSM-5 sample with  $\text{Si}/\text{Al} = 507$ ) with alumina or silica binders, was shown to have a dramatic impact on (1) the concentration in acid sites, (2) the access to the zeolite micropores and (3) the overall catalytic performance. However, the observation and quantification of these effects could not be reached by standard characterization techniques, whose sensitivity appeared to be too low to rank the properties of samples based on a  $\text{Si}/\text{Al}=507$  zeolite. Fluorescence microscopy appeared to be a key tool to quantify and localize acidity evolutions, on full catalyst pellets level using CLSM and on the single crystal level using NASCA. DFT calculations provided atomic scale information about the processes that are likely at the origin of the observed features.

The phenomena shown to take place thanks to our combined experimental and theoretical approaches are summarized in Scheme 3. For both families of binders, the resulting properties of the shaped zeolite are the result of a complex interplay between the zeolite and the binder. Migration of ions from and to the binder to the zeolite are shown to take place. On top of this,

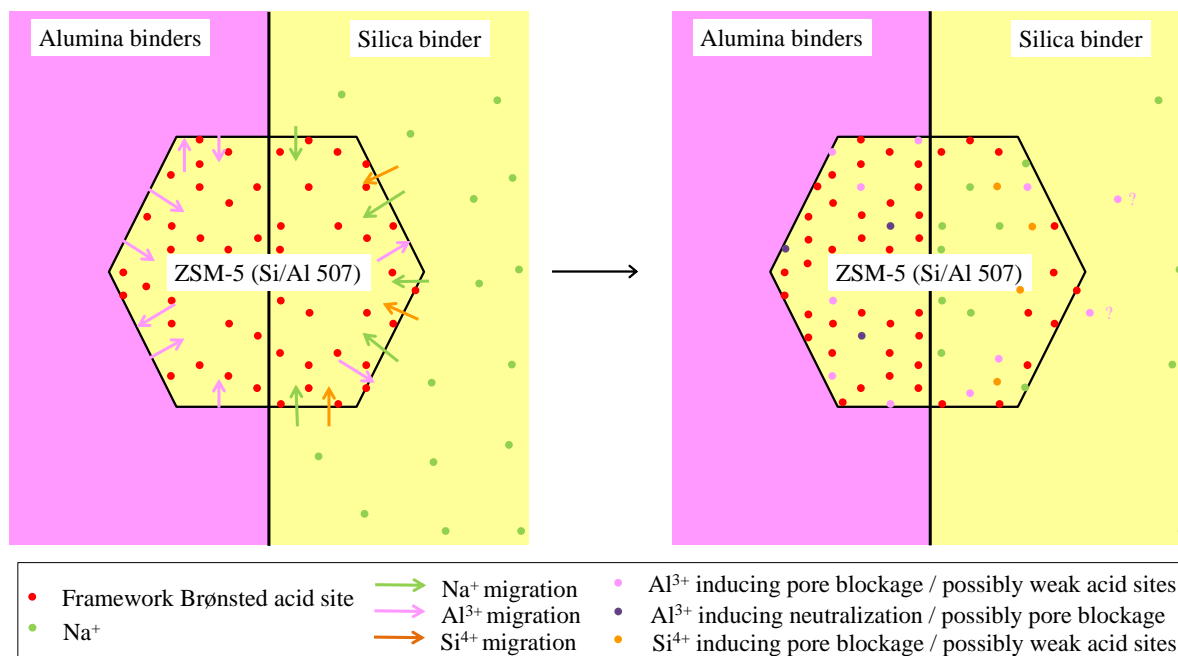
NASCA reveals a strong heterogeneity of the Z-507 crystals even before shaping in terms of reactivity with respect to furfurylic alcohol, that induces a variability of their response to shaping.

In the case of alumina,  $\text{Al}^{3+}$  cations (modeled in DFT by  $\text{Al}(\text{OH})_3(\text{H}_2\text{O})$  monomers) are stabilized both at the external surface of ZSM-5 and in the pore system, inducing pore blockage, but also reacting with framework sites (i) to neutralize some of the bridging OH-groups  $\text{Si}(\text{OH})-\text{Al}$ , (ii) to generate mild Brønsted acid sites such as  $\text{Al}(\text{H}_2\text{O})$ , pseudo-bridging silanols, and  $\mu_2\text{-Al-OH}$ , (iii) generate  $\text{Si}(\text{OH})-\text{Al}$  when filling defects of the framework. Dealumination may not be fully excluded, but the net balance is believed to be in favor of the alumination process. Experimentally, a significant difference in acidity was found depending on the boehmite and alumina binders and shaping procedure chosen. The acidity decreases when going from a  $\gamma\text{-Al}_2\text{O}_3$  (calcined boehmite), boehmite dispersed in an acidic medium, then boehmite shaped without acid. The differences are likely linked to the concentration in alumina monomers, depending on the reactivity of the binder ions in the shaping medium.

In the case of silica, sodium is seen to play a major role explaining the vanishing of the acidity properties. A thermodynamic driving force exists, that induces its migration from the binder to the zeolite crystal core. Dealumination and migration of silica monomers (modeled as  $\text{Si}(\text{OH})_4$ ) are likely and explain the observed pore blockage. In the future, the transposition of such an investigation to other samples with lower Si/Al ratio, and with more homogeneous distribution of acid sites from one crystallite to another, will be beneficial. In this case standard techniques will give quantitative information, that will be significantly enriched thanks to the mapping of active sites offered by fluorescence microscopy techniques.

However, our observations and their atomic-scale assignments already open the door to a better control of the evolution of the properties of the zeolite after shaping, which is crucial to

transfer the benefit of the laboratory scale catalyst design, to the practical implementation of these solids.



Scheme 3. Simplified representation of the main phenomena taking place during shaping of the Z-507 sample, as revealed by fluorescence microscopy, textural analysis and DFT calculations. Left: fictive state with independent components (zeolite, binder) and observed migrations. Right: state after shaping and thermal treatment. A model of the zeolite particle is chosen, the heterogeneity of the initial Z-507 crystals is not depicted. Migrating species are named according to the cation they contain, without further detail on the precise nature (level of hydroxylation and protonation state).

## ASSOCIATED CONTENT

**Supporting Information.** Supporting-Information.pdf contains information about physisorption isotherms, infra-red spectra, xylene isomerization, DFT calculations. gif3D\_figure 3A.gif and Gif3D\_figure\_3D.gif are 3D projections rotating around their central axis of CLSM measurements for the Z-507-Al sample.

## AUTHOR INFORMATION

### Corresponding Authors

\*Maarten Roeffaers, KU Leuven, [maarten.roeffaers@biw.kuleuven.be](mailto:maarten.roeffaers@biw.kuleuven.be)

\* Céline Chizallet, IFP Energies nouvelles, [celine.chizallet@ifpen.fr](mailto:celine.chizallet@ifpen.fr)

### **Author Contributions**

The manuscript was written through contributions of all authors. All authors have given approval to the final version of the manuscript.

### **ACKNOWLEDGMENT**

HPC resources were used from GENCI-IDRIS (Grant A0060806134), and IFPEN (ENER440).

## References

- (1) Vermeiren, W.; Gilson, J. P., Impact of Zeolites on the Petroleum and Petrochemical Industry, *Topics Catal.* **2009**, *52*, 1131-1161.
- (2) Ennaert, T.; Van Aelst, J.; Dijkmans, J.; De Clercq, R.; Schutyser, W.; Dusselier, M.; Verboekend, D.; Sels, B. F., Potential and Challenges of Zeolite Chemistry in the Catalytic Conversion of Biomass, *Chem. Soc. Rev.* **2016**, *45*, 584-611.
- (3) Mitchell, S.; Michels, N.-L.; Perez-Ramirez, J., From Powder to Technical Body: the Undervalued Science of Catalyst Scale Up, *Chem. Soc. Rev.* **2013**, *42*, 6094-6112.
- (4) Murzin, D. Y., On Spatial Control in Heterogeneous Multifunctional Catalysts, *Catal. Lett.* **2017**, *147*, 613-621.
- (5) Bingre, R.; Louis, B.; Nguyen, P., An Overview on Zeolite Shaping Technology and Solutions to Overcome Diffusion Limitations, *Catalysts* **2018**, *8*, 163.
- (6) Michels, N.-L.; Mitchell, S.; Pérez-Ramírez, J., Effects of Binders on the Performance of Shaped Hierarchical MFI Zeolites in Methanol-to-Hydrocarbons, *ACS Catal.* **2014**, *4*, 2409-2417.
- (7) Pérez-Uriarte, P.; Gamero, M.; Ateka, A.; Díaz, M.; Aguayo, A. T.; Bilbao, J., Effect of the Acidity of HZSM-5 Zeolite and the Binder in the DME Transformation to Olefins, *Ind. Eng. Chem. Res.* **2016**, *55*, 1513-1521.
- (8) Yang, K.; Zhang, D.; Zou, M.; Yu, L.; Huang, S., The Known and Overlooked Sides of Zeolite-Extrudate Catalysts, *ChemCatChem* **2021**, *13*, 1414-1423.
- (9) Whiting, G. T.; Meirer, F.; Mertens, M. M.; Bons, A.-J.; Weiss, B. M.; Stevens, P. A.; de Smit, E.; Weckhuysen, B. M., Binder Effects in SiO<sub>2</sub>- and Al<sub>2</sub>O<sub>3</sub>-Bound Zeolite ZSM-5-Based Extrudates as Studied by Microspectroscopy, *ChemCatChem* **2015**, *7*, 1312-1321.
- (10) Mäurer, T.; Müller, S. P.; Kraushaar-Czarnetzki, B., Aggregation and Peptization Behavior of Zeolite Crystals in Sols and Suspensions, *Ind. Eng. Chem. Res.* **2001**, *40*, 2573-2579.
- (11) Itani, L.; Valtchev, V.; Patarin, J.; Rigolet, S.; Gao, F.; Baudin, G., Centimeter-Sized Zeolite Bodies of Intergrown Crystals: Preparation, Characterization and Study of Binder Evolution, *Microporous Mesoporous Mater.* **2011**, *138*, 157-166.
- (12) Mitchell, S.; Michels, N.-L.; Kunze, K.; Pérez-Ramírez, J., Visualization of Hierarchically Structured Zeolite Bodies from Macro to Nano Length Scales, *Nature Chem.* **2012**, *4*, 825-831.
- (13) Whiting, G. T.; Chung, S.-H.; Stosic, D.; Chowdhury, A. D.; van der Wal, L. I.; Fu, D.; Zecevic, J.; Travert, A.; Houben, K.; Baldus, M.; Weckhuysen, B. M., Multiscale Mechanistic Insights of Shaped Catalyst Body Formulations and Their Impact on Catalytic Properties, *ACS Catal.* **2019**, *9*, 4792-4803.
- (14) Lakiss, L.; Gilson, J.-P.; Valtchev, V.; Mintova, S.; Vicente, A.; Vimont, A.; Bedard, R.; Abdo, S.; Bricker, J., Zeolites in a Good Shape: Catalyst Forming by Extrusion Modifies their Performances, *Microporous Mesoporous Mater.* **2020**, *299*, 110114.
- (15) Wodarz, S.; Slaby, N. A.; Zimmermann, M. C.; Otto, T. N.; Holzinger, J.; Skibsted, J.; Zevaco, T. A.; Pitter, S.; Sauer, J., Shaped Hierarchical H-ZSM-5 Catalysts for the Conversion of Dimethyl Ether to Gasoline, *Ind. Eng. Chem. Res.* **2020**, *59*, 17689-17707.
- (16) Velthoen, M. E. Z.; Lucini Paioni, A.; Teune, I. E.; Baldus, M.; Weckhuysen, B. M., Matrix Effects in a Fluid Catalytic Cracking Catalyst Particle: Influence on Structure, Acidity, and Accessibility, *Chem. Eur. J.* **2020**, *26*, 11995-12009.
- (17) Kuehl, G. H.; Timken, H. K. C., Acid Sites in Zeolite Beta: Effects of Ammonium Exchange and Steaming, *Microporous Mesoporous Mater.* **2000**, *35-36*, 521-532.
- (18) Bordiga, S.; Lamberti, C.; Bonino, F.; Travert, A.; Thibault-Starzyk, F., Probing Zeolites by Vibrational Spectroscopies, *Chem. Soc. Rev.* **2015**, *44*, 7262-7341.
- (19) Ristanovic, Z.; Kerssens, M. M.; Kubarev, A. V.; Hendriks, F. C.; Dedecker, P.; Hofkens, J.; Roeffaers, M. B.; Weckhuysen, B. M., High-Resolution Single-Molecule Fluorescence Imaging of Zeolite Aggregates within Real-Life Fluid Catalytic Cracking Particles, *Angew. Chem. Int. Edit.* **2015**, *54*, 1836-1840.
- (20) Whiting, G. T.; Chowdhury, A. D.; Oord, R.; Paalanen, P.; Weckhuysen, B. M., The Curious Case of Zeolite-Clay/Binder Interactions and their Consequences for Catalyst Preparation, *Faraday Discuss.* **2016**, *188*, 369-386.

- (21) Roeffaers, M. B. J.; Sels, B. F.; Uji-i, H.; Blanpain, B.; L'Hoëst, P.; Jacobs, P. A.; De Schryver, F. C.; Hofkens, J.; De Vos, D. E., Space- and Time-Resolved Visualization of Acid Catalysis in ZSM-5 Crystals by Fluorescence Microscopy, *Angew. Chem. Int. Ed.* **2007**, *46*, 1706-1709.
- (22) Roeffaers, M. B. J.; Ameloot, R.; Baruah, M.; Uji-i, H.; Bulut, M.; De Cremer, G.; Müller, U.; Jacobs, P. A.; Hofkens, J.; Sels, B. F.; De Vos, D. E., Morphology of Large ZSM-5 Crystals Unraveled by Fluorescence Microscopy, *J. Am. Chem. Soc.* **2008**, *130*, 5763–5772.
- (23) Thibault-Starzyk, F.; Stan, I.; Abello, S.; Bonilla, A.; Thomas, K.; Fernadez, C.; Gilson, J. P.; Perez-Ramirez, J., Quantification of Enhanced Acid Site Accessibility in Hierarchical Zeolites – The Accessibility Index, *J. Catal.* **2009**, *264*, 11-14.
- (24) Chen, N.-Y.; Liu, M.-C.; Yang, S.-C.; Sheu, H.-S.; Chang, J.-R., Impacts of Binder-Zeolite Interactions on the Structure and Surface Properties of NaY–SiO<sub>2</sub> Extrudates, *Ind. Eng. Chem. Res.* **2015**, *54*, 8456-8468.
- (25) Zheng, Y.; Song, J.; Xu, X.; He, M.; Wang, Q.; Yan, L., Peptization Mechanism of Boehmite and Its Effect on the Preparation of a Fluid Catalytic Cracking Catalyst, *Ind. Eng. Chem. Res.* **2014**, *53*, 10029-10034.
- (26) Xue, N.; Olindo, R.; Lercher, J. A., Impact of Forming and Modification with Phosphoric Acid on the Acid Sites of HZSM-5, *J. Phys. Chem. C* **2010**, *114*, 15763-15770.
- (27) Sheng, X.; Zhou, Y.; Kong, J.; Zhang, Y.; Zhang, Z.; Zhou, S., Influence of Pseudo-Boehmite Binder Modified Dealuminated Mordenite on Friedel–Crafts Alkylation, *Journal of Porous Materials* **2015**, *22*, 179-185.
- (28) Kubicek, N.; Vaudry, F.; Chiche, B. H.; Hudec, P.; Di Renzo, F.; Schulz, P.; Fajula, F., Stabilization of Zeolite Beta for FCC Application by Embedding in Amorphous Matrix, *Appl. Catal. A* **1998**, *175*, 159-171.
- (29) Shihabi, D. S.; Garwood, W. E.; Chu, P.; Miale, J. N.; Lago, R. M.; Chu, C. T. W.; Chang, C. D., Aluminum Insertion into High-Silica Zeolite Frameworks: II. Binder Activation of High-Silica ZSM-5, *J. Catal.* **1985**, *93*, 471-474.
- (30) Martin, A.; Berndt, H.; Lohse, U.; Wolf, U., Effect of Si : Al Ratio and Type of Binder on the Catalytic Properties of HZSM-5 Catalysts, *J. Chem. Soc., Faraday Trans.* **1993**, *89*, 1277-1282.
- (31) Verboekend, D.; Chabaneix, A. M.; Thomas, K.; Gilson, J.-P.; Pérez-Ramírez, J., Mesoporous ZSM-22 Zeolite Obtained by Desilication: Peculiarities Associated with Crystal Morphology and Aluminium Distribution, *CrystEngComm* **2011**, *13*, 3408-3416.
- (32) Vogt, E. T. C.; Weckhuysen, B. M., Fluid Catalytic Cracking: Recent Developments on the Grand Old Lady of Zeolite Catalysis, *Chem. Soc. Rev.* **2015**, *44*, 7342-7370.
- (33) Bertocini, F.; Bonduelle-Skrzypcak, A.; Francis, J.; Guillon, E., Hydrocracking, In *Catalysis by transition metal sulphides: from molecular theory to industrial applications*; Toulhoat, H., Raybaud, P., Eds.; Editions Technip: 2013, p 609-677.
- (34) Euzen, P.; Raybaud, P.; Krokidis, X.; Toulhoat, H.; Loarer, J. L.; Jolivet, J.-P.; Froidefond, C., Alumina, In *Handbook of Porous Solids*; Schüth, F., Sing, K. S. W., Weitkamp, J., Eds.; Wiley-VCH: Weinheim, 2002.
- (35) Bok, T. O.; Andriako, E. P.; Knyazeva, E. E.; Konnov, S. V.; Ivanova, I. I., Influence of the Binder Type on the Properties of Nanocrystalline Zeolite Beta-Based Catalysts for Benzene Alkylation with Propylene, *Petroleum Chemistry* **2018**, *58*, 833-840.
- (36) Liu, K.-L.; Kubarev, A. V.; Van Loon, J.; Uji-i, H.; De Vos, D. E.; Hofkens, J.; Roeffaers, M. B. J., Rationalizing Inter- and Intracrystal Heterogeneities in Dealuminated Acid Mordenite Zeolites by Stimulated Raman Scattering Microscopy Correlated with Super-resolution Fluorescence Microscopy, *ACS Nano* **2014**, *8*, 12650-12659.
- (37) Kubarev, A. V.; Janssen, K. P. F.; Roeffaers, M. B. J., Noninvasive Nanoscopy Uncovers the Impact of the Hierarchical Porous Structure on the Catalytic Activity of Single Dealuminated Mordenite Crystals, *ChemCatChem* **2015**, *7*, 3646-3650.
- (38) Janssen, K. P. F.; De Cremer, G.; Neely, R. K.; Kubarev, A. V.; Van Loon, J.; Martens, J. A.; De Vos, D. E.; Roeffaers, M. B. J.; Hofkens, J., Single Molecule Methods for the Study of Catalysis: from Enzymes to Heterogeneous Catalysts, *Chem. Soc. Rev.* **2014**, *43*, 990-1006.
- (39) Kennes, K.; Demaret, C.; Van Loon, J.; Kubarev, A. V.; Fleury, G.; Sliwa, M.; Delpoux, O.; Maury, S.; Harbuzaru, B.; Roeffaers, M. B. J., Assessing Inter and Intra-particle Heterogeneity in Alumina-poor H-ZSM-5 Zeolites, *ChemCatChem* **2017**, *9*, 3440-3445.

- (40) Roeffaers, M. B. J.; De Cremer, G.; Libeert, J.; Ameloot, R.; Dedecker, P.; Bons, A.-J.; Bückins, M.; Martens, J. A.; Sels, B. F.; De Vos, D. E.; Hofkens, J., Super-Resolution Reactivity Mapping of Nanostructured Catalyst Particles, *Angew. Chem. Int. Ed.* **2009**, *48*, 9285-9289.
- (41) Chizallet, C., Toward the Atomic Scale Simulation of Intricate Acidic Aluminosilicate Catalysts, *ACS Catal.* **2020**, *10*, 5579-5601.
- (42) Chizallet, C., Achievements and Expectations in the Field of Computational Heterogeneous Catalysis in an Innovation Context, *Topics Catal.* **2022**, *65*.
- (43) Treps, L.; Gomez, A.; De Bruin, T.; Chizallet, C., Environment, Stability and Acidity of External Surface Sites of Silicalite-1 and ZSM-5 Micro- and Nano-Slabs, -Sheets and -Crystals, *ACS Catal.* **2020**, *10*, 3297-3312.
- (44) Treps, L.; Demaret, C.; Wisser, D.; Harbuzaru, B.; Méthivier, A.; Guillon, E.; Benedis, D. V.; Gomez, A.; De Bruin, T.; Rivallan, M.; Catita, L.; Lesage, A.; Chizallet, C., Spectroscopic Expression of the External Surface Sites of H-ZSM-5, *J. Phys. Chem. C* **2021**, *125*, 2163-2181.
- (45) Emeis, C. A., Determination of Integrated Molar Extinction Coefficients for Infrared Absorption Bands of Pyridine Adsorbed on Solid Acid Catalysts, *J. Catal.* **1993**, *141*, 347-354.
- (46) Peter, D.; Sam, D.; Robert, K. N.; Jin, Z., Localizer: Fast, Accurate, Open-Source, and Modular Software Package for Superresolution Microscopy, *Journal of Biomedical Optics* **2012**, *17*, 1-5.
- (47) Perdew, J.; Burke, K.; Ernzerhof, M., Generalized Gradient Approximation Made Simple, *Phys. Rev. Lett.* **1996**, *77*, 3865-3868.
- (48) Kresse, G.; Hafner, J., Ab Initio Molecular-Dynamics Simulation of the Liquid-Metal-Amorphous-Semiconductor Transition in Germanium, *Phys. Rev. B* **1994**, *49*, 14251-14269.
- (49) Kresse, G.; Furthmüller, J., Efficiency of Ab-Initio Total Energy Calculations for Metals and Semiconductors using a Plane-Wave Basis Set, *Comput. Mat. Sci.* **1996**, *6*, 15-50.
- (50) Kresse, G.; Joubert, D., From Ultrasoft Pseudopotentials to the Projector Augmented-Wave Method, *Phys. Rev. B* **1999**, *59*, 1758-1775.
- (51) Steinmann, S. N.; Corminboeuf, C., Comprehensive Benchmarking of a Density-Dependent Dispersion Correction, *J Chem Theory Comput* **2011**, *7*, 3567-3577.
- (52) Tielens, F.; Gervais, C.; Lambert, J. F.; Mauri, F.; Costa, D., Ab Initio Study of the Hydroxylated Surface of Amorphous Silica: A Representative Model, *Chem. Mater.* **2008**, *20*, 3336-3344.
- (53) Digne, M.; Sautet, P.; Raybaud, P.; Euzen, P.; Toulhoat, H., Hydroxyl Groups on Gamma-Alumina Surfaces: a DFT Study, *J. Catal.* **2002**, *211*, 1-5.
- (54) Digne, M.; Sautet, P.; Raybaud, P.; Euzen, P.; Toulhoat, H., Use of DFT to Achieve a Rational Understanding of Acid-Basic Properties of Gamma-Alumina Surfaces, *J. Catal.* **2004**, *226*, 54-68.
- (55) Digne, M.; Raybaud, P.; Sautet, P.; Guillaume, D.; Toulhoat, H., Quantum Chemical and Vibrational Investigation of Sodium Exchanged gamma-Alumina Surfaces, *Phys. Chem. Chem. Phys.* **2007**, *9*, 2577-2582.
- (56) Galarneau, A.; Mehlhorn, D.; Guenneau, F.; Coasne, B.; Villemot, F.; Minoux, D.; Aquino, C.; Dath, J. P., Specific Surface Area Determination for Microporous/Mesoporous Materials: The Case of Mesoporous FAU-Y Zeolites, *Langmuir* **2018**, *34*, 14134-14142.
- (57) Galarneau, A.; Villemot, F.; Rodriguez, J.; Fajula, F.; Coasne, B., Validity of the t-Plot Method to Assess Microporosity in Hierarchical Micro/Mesoporous Materials, *Langmuir* **2014**, *30*, 13266-13274.
- (58) Hoffmann, P.; Lobo, J. A., Identification of Diverse Silanols on Protonated ZSM-5 Zeolites by Means of FTIR Spectroscopy, *Microporous Mesoporous Mater.* **2007**, *106*, 122-128.
- (59) Roeffaers, M. B. J.; Ameloot, R.; Bons, A.-J.; Mortier, W.; De Cremer, G.; de Kloe, R.; Hofkens, J.; De Vos, D. E.; Sels, B. F., Relating Pore Structure to Activity at the Subcrystal Level for ZSM-5: An Electron Backscattering Diffraction and Fluorescence Microscopy Study, *J. Am. Chem. Soc.* **2008**, *130*, 13516-13517.
- (60) Benco, L.; Demuth, T.; Hafner, J.; Kutschka, F.; Toulhoat, H., Extraframework Aluminum Species in Zeolites: Ab Initio Molecular Dynamics Simulation of Gmelinite, *J. Catal.* **2002**, *209*, 480-488.
- (61) Chizallet, C.; Raybaud, P., Pseudo-Bridging Silanols as Versatile Brønsted Acid Sites of Amorphous Aluminosilicates Surfaces, *Angew. Chem. Int. Ed.* **2009**, *48*, 2891-2893.



- (62) Leydier, F.; Chizallet, C.; Chaumonnot, A.; Digne, M.; Soyer, E.; Quoineaud, A. A.; Costa, D.; Raybaud, P., Brønsted Acidity of Amorphous Silica–Alumina: The Molecular Rules of Proton Transfer, *J. Catal.* **2011**, *284*, 215-229.
- (63) Valla, M.; Rossini, A. J.; Caillot, M.; Chizallet, C.; Raybaud, P.; Digne, M.; Chaumonnot, A.; Lesage, A.; Emsley, L.; van Bokhoven, J. A.; Coperet, C., Atomic Description of the Interface between Silica and Alumina in Aluminosilicates through Dynamic Nuclear Polarization Surface-Enhanced NMR Spectroscopy and First-Principles Calculations, *J. Am. Chem. Soc.* **2015**, *137*, 10710-10719.
- (64) Rey, J.; Raybaud, P.; Chizallet, C., Ab Initio Simulation of the Acid Sites at the External Surface of Zeolite Beta, *ChemCatChem* **2017**, *9*, 2176-2185.
- (65) Chizallet, C.; Raybaud, P., Acidity of Amorphous Silica–Alumina: From Coordination Promotion of Lewis Sites to Proton Transfer, *ChemPhysChem* **2010**, *11*, 105-108.
- (66) Leydier, F.; Chizallet, C.; Costa, D.; Raybaud, P., CO Adsorption on Amorphous Silica–Alumina: Electrostatic or Brønsted Acidity Probe?, *Chem. Commun.* **2012**, *48*, 4076-4078.
- (67) Leydier, F.; Chizallet, C.; Costa, D.; Raybaud, P., Revisiting Carbenium Chemistry on Amorphous Silica-Alumina: Unraveling their Milder Acidity as Compared to Zeolites, *J. Catal.* **2015**, *325*, 35-47.
- (68) Larmier, K.; Chizallet, C.; Maury, S.; Cadran, N.; Abboud, J.; Lamic-Humblot, A. F.; Marceau, E.; Lauron-Pernot, H., Isopropanol Dehydration on Amorphous Silica-Alumina: Synergy of Bronsted and Lewis Acidities at Pseudo-Bridging Silanols, *Angew. Chem. Int. Ed.* **2017**, *56*, 230-234.
- (69) Larmier, K.; Nicolle, A.; Chizallet, C.; Cadran, N.; Maury, S.; Lamic-Humblot, A.-F.; Marceau, E.; Lauron-Pernot, H., Influence of Coadsorbed Water and Alcohol Molecules on Isopropyl Alcohol Dehydration on  $\gamma$ -Alumina: Multiscale Modeling of Experimental Kinetic Profile, *ACS Catal.* **2016**, *6*, 1905-1920.
- (70) Larmier, K.; Chizallet, C.; Cadran, N.; Maury, S.; Abboud, J.; Lamic-Humblot, A.-F.; Marceau, E.; Lauron-Pernot, H., Mechanistic Investigation of Isopropanol Conversion on Alumina Catalysts: Location of Active Sites for Alkene/Ether Production, *ACS Catal.* **2015**, *5*, 4423-4437.
- (71) Silaghi, M.-C.; Chizallet, C.; Sauer, J.; Raybaud, P., Dealumination Mechanisms of Zeolites and Extra-Framework Aluminum Confinement, *J. Catal.* **2016**, *339*, 242-255.
- (72) Stanciakova, K.; Ensing, B.; Göttl, F.; Buló, R. E.; Weckhuysen, B. M., Cooperative Role of Water Molecules during the Initial Stage of Water-Induced Zeolite Dealumination, *ACS Catal.* **2019**, *9*, 5119-5135.
- (73) Nielsen, M.; Brogaard, R. Y.; Falsig, H.; Beato, P.; Swang, O.; Svelle, S., Kinetics of Zeolite Dealumination: Insights from H-SSZ-13, *ACS Catal.* **2015**, *5*, 7131-7139.
- (74) Nielsen, M.; Hafreager, A.; Brogaard, R. Y.; De Wispelaere, K.; Falsig, H.; Beato, P.; Van Speybroeck, V.; Svelle, S., Collective Action of Water Molecules in Zeolite Dealumination, *Catal. Sci. Technol.* **2019**, *9*, 3721-3725.
- (75) Nampi, P. P.; Ghosh, S.; Warriar, K. G., Calcination and Associated Structural Modifications in Boehmite and their Influence on High Temperature Densification of Alumina, *Ceramics International* **2011**, *37*, 3329-3334.
- (76) Krokidis, X.; Raybaud, P.; Gobichon, A. E.; Rebours, B.; Euzen, P.; Toulhoat, H., Theoretical Study of the Dehydration Process of Boehmite to gamma-Alumina, *J. Phys. Chem. B* **2001**, *105*, 5121-5130.
- (77) Valtchev, V.; Majano, G.; Mintova, S.; Perez-Ramirez, J., Tailored Crystalline Microporous Materials by Post-Synthesis Modification, *Chem. Soc. Rev.* **2013**, *42*, 263-290.
- (78) Uguina, M. A.; Sotelo, J. L.; Serrano, D. P., Toluene Disproportionation over ZSM-5 Zeolite: Effects of Crystal Size, Silicon-to-Aluminum Ratio, Activation Method and Pelletization, *Appl. Catal.* **1991**, *76*, 183-198.

## Graphical TOC

